Quantifying daily NO_x and CO_2 emissions from Wuhan using satellite observations from TROPOMI and OCO-2

Qianqian Zhang[1,2], K. Folkert Boersma[1,3], Bin Zhao[4], Henk Eskes[3], Cuihong Chen[5], Haotian Zheng[4], Xingying Zhang[2]

[1] Wageningen University, Environmental Science Group, Wageningen, the Netherlands
[2] Key Laboratory of Radiometric Calibration and Validation for Environmental Satellites, Innovation Center for Fengyun Meteorological Satellite (FYSIC), National Satellite Meteorological Center, China Meteorology Administration, Beijing, 100081, China
[3] Royal Netherlands Meteorological Institute, De Bilt, the Netherlands
[4] State Key Joint Laboratory of Environmental Simulation and Pollution Control, School of environment, Tsinghua University, Beijing 100084, China
[5] Satellite Application Center for Ecology and Environment, Ministry of Ecology and Environment of the People's Republic of China, Beijing, 100094, China

Correspondence to: K. Folkert Boersma, folkert.boersma@wur.nl, Qianqian Zhang, zhangqq@cma.gov.cn

Abstract. Quantification and control of NO_x and CO_2 emissions are important across the world to limit adverse climate change and improve air quality. We present a new top-down method, an improved superposition column model to estimate day-to-day NO_x and CO_2 emissions from the large city of Wuhan, China, located in a polluted background. The laststd released version 2.3.1 TROPOMI NO_2 columns and the version 10r of the OCO-2 observed CO_2 mixing ratio are employed. We predictedquantified daily NO_x and CO_2 emissions from Wuhan between September 2019 to October 2020 with uncertainty of 31 % and 43 %, comparing to the 39% and 49% with the earlier v1.3 TROPOMI data, respectively. Our estimated estimated NO_x and CO_2 emissions from Wuhan are verified against bottom-up inventories with small deviations (< 3 % for 2019 mean, ranging from -20 % to 48 % on daily basis). Based on the estimated CO_2 emissions, we also predicted daily CO_2 column mixing ratio enhancements, which match well with OCO-2 observations (< 5 % bias, within ±0.3 ppm). We capture the day-to-day variation of NO_x and CO_2 emissions from Wuhan in 2019–2020, which does not reveal a substantial 'weekend reduction' but does show a clear 'holiday reduction' in the NO_x and CO_2 emissions. Our method also quantifies the abrupt decrease and slow rebound of NO_x and CO_2 emissions due to the Wuhan lockdown in early 2020. This work demonstrates the improved superposition model to be a promising new tool for the quantification of city NO_x and CO_2 emissions, allowing policy makers to gain real-time information into spatial-temporal emission patterns and the effectiveness of carbon and nitrogen regulation in urban environments.

1 Introduction

Fossil fuel combustion by power plants, industrial activities, transportation, and residential energy use sectors leads to emission of nitrogen oxides (NO_x = NO + NO_2) as well as carbon dioxide (CO_2). Traditional bottom-up NO_x and CO_2 emission estimates have a lag in time of several ~~years, because~~years because it takes time to access and compile accurate information on energy consumption and the emission factors (Lamsal et al., 2011; Liu et al., 2020a).

For decades satellites have been continuously providing information of NO_2 distributions and trends with good quality, and satellite data is widely used to quantify NO_x emissions and changes (Lamsal et al., 2010; Visser et al., 2019; Zhang et al., 2020; Zhang et al., 2021). Based on satellite retrieved NO_2 data, previous studies quantified long-term mean (monthly, yearly or multi-yearly) NO_x emissions on global and regional scales (Lamsal et al., 2011; Visser et al., 2019). Beirle et al. (2011) analyzed ~~downwind~~ plumes of satellite NO_2 columns downwind of strong sources averaged for~~on~~ each wind direction, and then inferred NO_x emissions from isolated large point sources and megacities. Inspired by this idea, Lorente et al. (2019) analyzed the increase of NO_2 along with the wind over the extensive pollution source of Paris. The build-up of NO_2 over the city observed from space, in combination with information on wind speed and direction allows to obtain day-by-day (sub-)urban NO_x emission estimates and lifetimes as long as the city is under a clear sky and winds are relatively constant in time. This approach does not need burdensome inverse modelling computations and opens possibilities for rapid and direct monitoring of NO_x emissions from space.

In contrast to NO_x, it is challenging to infer accurate localized anthropogenic CO_2 emissions from satellite CO_2 retrievals. One reason is that the background CO_2 concentration is orders of magnitude higher than the enhancement caused by anthropogenic emissions, reflecting the long atmospheric lifetime of CO_2 (Reuter et al., 2014; 2019). Another reason is that the spatial and temporal coverage of current CO_2 sensors is too sparse to allow substantial averaging of noisy signals by revisiting of scenes, precluding detailed CO_2 emission estimation (Zheng et al., 2020a; Liu et al., 2020a). Using satellite NO_2 measurements to estimate anthropogenic NO_x emissions as the basis to infer anthropogenic CO_2 emission has been proposed in several studies (Reuter et al., 2019; Liu et al., 2020a; Berezin et al., 2013; Zheng et al., 2020a). However, to our knowledge there is no method that estimates day-to-day top-down CO_2 emission estimation on (sub-)city scale.

Here we revisit the method of Lorente et al. (2019) to improve our understanding of its potential and limitations and extend it to estimate city-scale daily NO_x and CO_2 emissions. We present an improved superposition model that considers the build-up of pollution over a source area as in Lorente et al. (2019), as well as the decay of NO_2 downwind of the source, but now also accounts for changes in the background NO_2 pollution along wind direction. The background NO_2 pollution was considered to remain constant in Lorente et al. (2019) for Paris, which is not surrounded by significant surface sources of NO_x pollution. Here we apply our improved method on a highly polluted urban area, the megacity of Wuhan in Hubei Province of

China, which, other than the relatively isolated city of Paris, is located in a polluted background with many surrounding surface pollution sources that potentially interfere with the build-up and decay of the NO_2 plume from Wuhan. Using this improved superposition model, together with ~~the~~ bottom-up information on the CO_2-to-NO_x emission ratio, we infer NO_x and predict CO_2 emissions on a day-by-day basis over a full year, from September 2019 to August 2020, and analyze the variation in emissions and NO_x chemical lifetime from day to day. Of particular interest are the reductions and subsequent rebound of NO_x and CO_2 emissions associated with the COVID-19 lockdown measures in Wuhan, which have been reported in other studies, and serve here as a useful check on the robustness of our method.

2 Data and Material

2.1 Satellite data

In this study, we use the newly released level-2, version 2.3.1 of the S-5P TROPOMI data (TROPOMI-v2.3.1) between September 2019 to August 2020. The S-5P (Sentinel-5 Precursor) satellite was launched in October 2017, and the TROPOMI (TROPOspheric Monitoring Instrument) on board provides tropospheric NO_2 columns with a unprecedented horizontal resolution up to 5.5 km × 3.5 km (as of 6 August 2019) and high signal-to-noise ratio (Griffin et al., 2019; Van Geffen et al., 2020). The v2.3.1 dataset is provided by S5P-PAL (S5P Science and Technology Product Algorithm Laboratory) (Eskes et al., 2021), and is dedicated to support the research on the impact of the COVID lockdown on air quality. Improved (residual) cloud pressures correct the low bias of v1.x data compared to OMI and ground-based measurements over east China (Wang et al., 2020; Liu et al., 2020b). In addition, an improved treatment for the surface albedo increases the columns for cloud-free scenes (Van Geffen et al., 2022). Compared to the earlier version, this dataset has 10–40 % higher tropospheric NO_2 columns over polluted scenes due to the improved cloud retrieval and other algorithm updates (Van Geffen et al., 2022; Riess et al., 2022). Over Wuhan we find an average increase (compared to the v1.3 data, hereinafter referred to as TROPOMI-v1.3) in tropospheric NO_2 column density of about 25 %, but there are also differences between the two versions in terms of spatial and temporal distribution ~~but the difference between the two versions changes spatially and temporally~~ (Fig. S2). According to Fig. S2, According to Fig. S2, the increase in v2.3.1 is much stronger over a polluted area (city center) and polluted period ~~the increase in TROPOMI v2.3.1 is much higher over polluted area (city center) and polluted period~~ (9 September and 3 October 2019). Since ~~that~~ the v1.x TROPOMI data is widely used in previous studies (e.g. Bauwens et al., 2020; Ding et al., 2020; Zhang et al., 2021), we also compared the estimated NO_x lifetime and emissions from the TROPOMI-v2.3.1 data and the TROPOMI-v1.3 data, which will be discussed in Sec. 3.1. ~~Improved (residual) cloud pressures correct the low bias of v1.x data compared to OMI and ground-based measurements over east China (Wang et al., 2020; Liu et al., 2020b). In addition, an improved treatment for the surface albedo increases the columns for cloud-free scenes (Van Geffen et al., 2022). For comparison (and to assess the impact of retrieval improvements on NO_x emission estimates), we also use version 1.3 data (TROPOMI v1.3) for 2019 to derive NO_x emissions from Wuhan.~~For the record, when estimating the NO_x emissions and lifetime over Wuhan, we scaled up the TROPOMI-v1.3 NO_2 columns by a factor of 1.6 to correct for th~~is~~e known -40 % bias in TROPOMI NO_2 data

as reported by Liu et al. (2020b). ~~Since previous studies have pointed out a low bias in the v1.x TROPOMI retrieval, especially over China (Griffin et al., 2019; Wang et al., 2020; Liu et al., 2020b), we scaled up the v1.3 NO_2 columns by a factor of 1.6 to correct for this known ~40 % bias in TROPOMI NO_2 data as reported by Liu et al. (2020b).~~

We sampled the TROPOMI NO_2 columns into 0.05° lat × 0.05° lon grid cells (~ 6 × 6 km^2). To assure good data quality, we filtered out the data with cloud radiance fractions greater than 0.5 (qa_value > 0.75)~~,~~ and obtain 81 clear-sky days with full TROPOMI NO_2 coverage over the Wuhan region in one full year.

The column-averaged dry air mole fraction of CO_2 (XCO_2) data provided by the Orbiting Carbon Observatory-2 (OCO-2) are also employed to verify the derived CO_2 emission inventory for Wuhan. We use the version 10r of the bias-corrected XCO_2 product (Gunson ~~M~~ and Eldering, 2020). The v10r OCO-2 XCO_2 product has high accuracy with single sounding precision of ~0.8 ppm over land and ~0.5 ppm over water, and RMS biases of 0.5–0.7 ppm over both land and water (Odell et al., 2021).

2.2 Bottom-up emission information

Bottom-up NO_x and CO_2 emission inventories are used to provide the ~~first guess~~first guess of NO_x emission spatial pattern (for NO_x, in the Supplement Material, Text S1 and Fig. S1) and to verify the top-down emissions. We use the Air Benefit and Attainment and Cost Assessment System Emission Inventory (ABACAS) (Zhao et al., 2013; Zhao et al., 2018; Zheng et al., 2019) , which provides NO_x and CO_2 emissions for the year 2019. The Multi-resolution Emission Inventory (MEIC) (Li et al., 2017) NO_x emissions for 2017 are also used.

2.3 Other input data

Besides the satellite data and bottom-up emission inventories, a set of other parameters are used to input into our improved superposition model. They include the hydroxyl radical (OH) concentration, the loss rate (k) of NO_x in the atmosphere, the $[NO_x]/[NO_2]$ ratio, and the wind field. We use the version 12.1 of GEOS-Chem model with a horizontal resolution of 0.25° × 0.3125° (~ 30 × 37.5 km^2) to provide the a priori guesses for chemical parameters relevant to daytime NO_x.~~The first three are from the GEOS-Chem chemical transport model,~~ ~~and t~~The wind field is from ERA5 (ECMWF Reanalysis v5), the fifth generation ECMWF (European Centre for Medium-Range Weather Forecasts) atmospheric reanalysis of the global climate (Hersbach et al., 2020). Detailed information on these data can be found in Text S2 (Supplementary Material)~~Detailed information of these data is seen in the supplement, Text S2~~. Considering that the wind field has a strong influence on the distribution of NO_2 column patterns, and thus on the NO_x emission estimation, we filter the TROPOMI NO_2 data based on the wind fields. After excluding the days with fluctuating wind direction (if wind direction changes more than 45 degrees in the hours before TROPOMI overpass) within the study domain, we finally obtain 50 days out of the ensemble of 81 valid satellite days between 1 September 2019 to 31 August 2020 to estimate NO_x and CO_2 emissions from Wuhan. The fraction of useful days is comparable to what Lorente et al. (2019) obtained for Paris, which is 27 days in 5 months.

2.4 NO_2 pattern fits: estimation of lifetime and emission

To ensure that the whole area of Wuhan is included, we determine our study domain as a circular region centered at 114° E, 30.7° N, with a diameter of ~186 km. It includes the whole area of Wuhan and the small city of Ezhou to the east of Wuhan, the southwest part of Huanggang and east part of Xiaogan (Fig. ~~S3~~S4, the red circle). We also do a sensitivity test to narrow the study area down to within the Third Ring Road of Wuhan to check the robustness of our model to the area size of study domain (Fig. ~~S3~~S4, the blue circle). For each day, we converted the two-dimensional NO_2 column map over the domain to a one-dimensional line density along the wind direction (Text S3) (Beirle, 2011; Lorente et al., 2019). NO_x emissions and lifetimes can be estimated through the fitting of the NO_2 line density over the domain.

Lorente et al. (2019) presented a superposition column model based on a simple column model (Jacob, 1999) to simulate NO_2 line density over Paris. They considered the build-up of NO_2 caused by spatially varying NO_x emissions from each cell and used the NO_2 line density value at the upwind end of the city to represent the background value, which they assumed to be constant over the city. This appears plausible if the background value would mostly represent free tropospheric NO_2 which has a longer lifetime than NO_2 in the oxidizing polluted boundary layer and varies smoothly according to models. Our method to simulate the NO_2 line density over the city is also based on the column model (Jacob, 1999), but differs from that of Lorente et al. (2019) in considering the background NO_2 value. Each cell along the wind direction is treated separately as a column model. Since ~~that~~ the satellite overpasses at around 13:30 local time, ~~when~~ NO_x is removed in the atmosphere dominantly through ~~a one~~the first-~~-~~order reaction with OH. NO_x emissions from the current cell contribute to the total line density through the build-up of NO_2 density within the cell and exponential decay of NO_2 downwind of the cell (Eq. (1)). It doesn't contribute to the upwind cells (Eq. (2)).

$$N_i(x) = \frac{E_i}{k}\left(1 - e^{-kL/u}\right) \times e^{-k(x-x_i)/u} \times \frac{[NO_2]}{[NO_x]} \quad for\ x > x_i \ , \tag{1}$$

$$N_i(x) = 0 \qquad for\ x \le x_i \ , \tag{2}$$

where N_i represents the NO_2 line density (molec ~~/~~cm~~-1~~) contributed from E_i in cell i, L is the length of each cell, i.e. 600000 cm; k is the loss rate (s^{-1}) of NO_x at 13:00 local time ($k = \frac{k'[OH]}{[NO_x]/[NO_2]}$); and u denotes the NO_2-density-weighted mean wind speed in unit of cm/s within planet boundary. We add up the contributions from each cell and the background value to model the overall NO_2 line density:

$$N(x) = \sum_{i=1}^{n} N_i(x) + b + \alpha x \ , \tag{3}$$

here, b represents the starting background value, equivalent to the mean NO_2 line density within the ~~-~~5 (for summer, spring and autumn) or 10 (for winter) cells ~~e folding distance(Liu et al., 2016)~~ upwind of x=0. α denotes the linear change of background value with distance along wind~~,~~ and represents the chemical decay of background NO_2 flowing into the polluted boundary layer over the city.

We fit the terms that drive $N(x)$ (i.e. E_i, k and α) with the fixed L, u and $[NO_x]/[NO_2]$ from external data, via a least-squares minimization to the TROPOMI observed line density $N_{TROPOMI}(x)$. For each day, we run the model 20 times randomly choosing OH concentration within the ±20% interval of GEOS-Chem simulated OH concentration. The mean value from the 5 sets of parameters E_i, k and α that best explain the observations over the city is the answer we are seeking for. The parameter that describes the decay of upwind NO_2 over the city, the α value, is determined by the difference of NO_2 line density between the end and start point of the study domain, $\alpha = \frac{(N_{31} - N_1)}{30L}$, and we allow it to change between $\pm\alpha$ in the fitting procedure. For the 50 days on average, the α value is $(-0.006 \pm 0.008) \times 10^{-22} molec\,cm^{-2}$. The α value being negative reflects the decay of upwind NO_2 pollution along the wind.

The assumption of a linearly decreasing NO_2 background is relevant under conditions when the city is in a polluted background. It accounts for decay of upwind NO_2 pollution arriving at the city when transported over and downwind of the city. In reality, upwind NO_2 pollution mixes in with the freshly emitted NO_x and is then subject to chemical decay (with non-linearities due to turbulent mixing and spatial heterogeneity in emissions). We acknowledge that our linear decrease of background NO_2 pollution is a severe simplification, but as shown in Fig. 1, compared to fitting results with a constant background value, we obtain a better correlation (up to 25%) and lower bias (nearly 50% lower) between fitted and observed NO_2 line densities when fitting with a linearly changing background value.

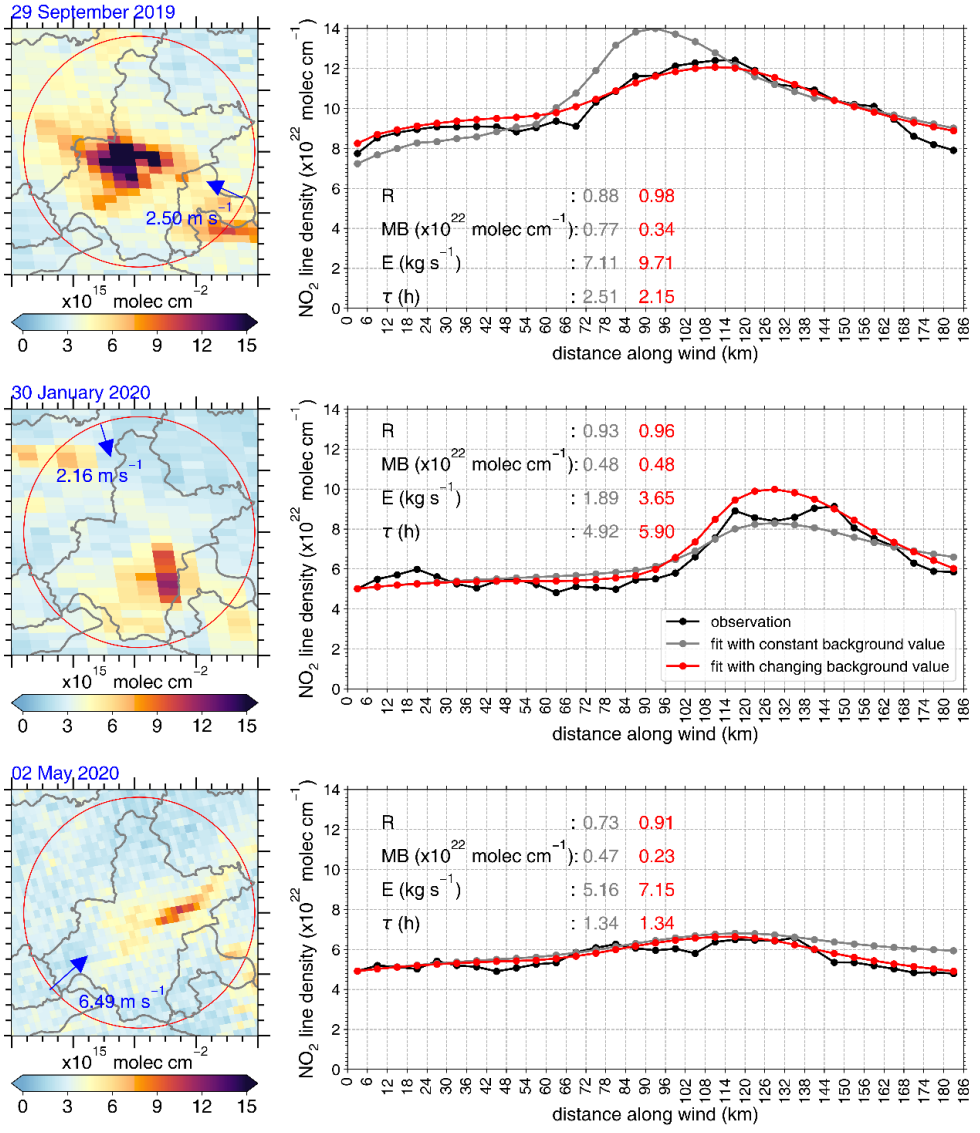
29 September 2019
2.50 m s-1
x10^15 molec cm^-2
0 3 6 9 12 15
NO2 line density (x10^22 molec cm^-1)
R : 0.88 0.98
MB (x10^22 molec cm^-1): 0.77 0.34
E (kg s^-1) : 7.11 9.71
τ (h) : 2.51 2.15
distance along wind (km)
30 January 2020
2.16 m s-1
x10^15 molec cm^-2
0 3 6 9 12 15
NO2 line density (x10^22 molec cm^-1)
R : 0.93 0.96
MB (x10^22 molec cm^-1): 0.48 0.48
E (kg s^-1) : 1.89 3.65
τ (h) : 4.92 5.90
observation
fit with constant background value
fit with changing background value
distance along wind (km)
02 May 2020
6.49 m s-1
x10^15 molec cm^-2
0 3 6 9 12 15
NO2 line density (x10^22 molec cm^-1)
R : 0.73 0.91
MB (x10^22 molec cm^-1): 0.47 0.23
E (kg s^-1) : 5.16 7.15
τ (h) : 1.34 1.34
distance along wind (km)

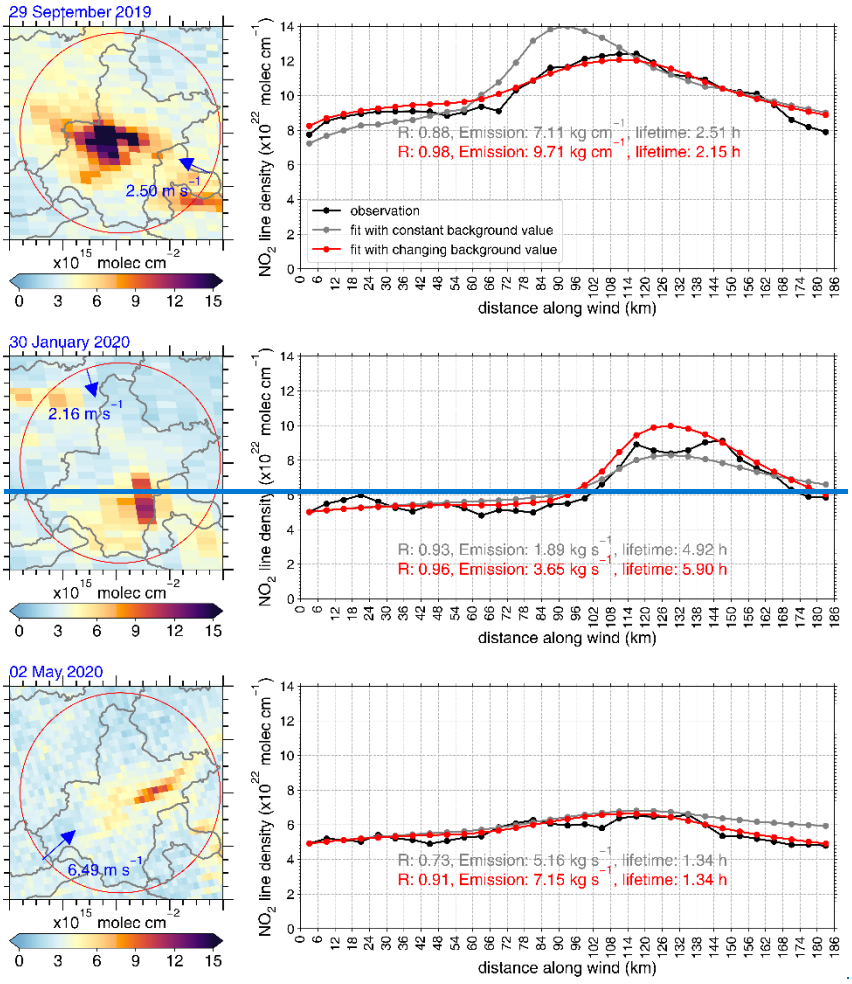

Figure 1: Tropospheric NO_2 columns over Wuhan on 29 September 2019, 30 January 2020 and 2 May 2020 (left, from top to bottom), the red circle inside each map defines the study domain. The corresponding NO_2 line densities along wind within the study domain are given in the right panel. For each day, the correlation coefficient (R) between the observed (black line) and fitted (grey and red lines) NO_2 line density are given. The fitted mean bias (MB), NO_x emissions (E) and NO_x lifetime (τ) are also displayed.

2.5 CO_2 emission estimation

City-scale CO_2 emissions are estimated through Eq. (4):

$$E_{CO_2} = E_{NO_x} \times Ratio_{CO_2-to-NO_x}, \quad (4)$$

The anthropogenic CO_2-to-NO_x emission ratio is provided by the ABACAS inventory, and amounts to ~591 gCO_2/gNO_x emitted from our study domain for the year 2019. In 2020, emissions from the transport sector have substantially decreased due to the lockdown measurements (Huang et al., 2021; Zheng et al., 2020c). The stronger decrease in transport NO_x emissions relative to decreases from other sectors are predicted to have led to an increase in the CO_2-to-NO_x emission ratio, for this ratio

is lowest in the transport sector (Zheng et al., 2020c). The monthly CO_2-to-NO_x emission ratio for Wuhan were calculated based on recent reports on sectoral NO_x emission in 2020 from Hubei Province (Zheng et al., 2021a). We then further calculated daily CO_2-to-NO_x emission ratio based on the monthly, daily and diurnal variation of CO_2 and NO_x emissions (Fig. ~~S5~~S5). The final daily CO_2-to-NO_x emission ratio for the study period displayed in Table S1 indeed shows increases in the CO_2-to-NO_x emission ratio of up to 20 % during the lockdown period in 2020 due to the reducing contribution from the transportation sector.

2.6 U~~u~~ncertainty in NO_x and CO_2 emission estimation

Uncertainties in quantifying NO_x and CO_2 emissions contain the systematic error in the TROPOMI NO_2 retrieval, bias in the assumed a priori OH concentration, NO_x/NO_2 ratio, CO_2-to-NO_x emission ratio, uncertainties in wind fields and the area of study domain. The v2.3.1 NO_2 column dataset ~~S5P-PAL~~ corrected the low bias in TROPOMI (v1.x) tropospheric NO_2 column over Eastern China by 15–100 % (Van Geffen et al., 2022), but there still remains an uncertainty of ~ ±20 %. ~~.~~ The CTMs have difficulty in simulating accurate OH concentration, but for > 90 % of the days, our fitted OH concentrations fall in ±20 % range around GEOS-Chem simulation, so the uncertainty in OH concentration is likely on the order of ±20 %. ~~-~~The difference between model simulated and observed NO_x/NO_2 ratio is less than 10 %, so we give an uncertainty in NO_x/NO_2 ratio of ±10 %. Uncertainty in CO_2-to-NO_x emission ratio comes from the errors in sectoral NO_x and CO_2 emissions, and we calculated that the uncertainty in CO_2-to-NO_x emission ratio is ±30 %. We use the NO_2-column-weighted mean instead of the arithmetic mean value to get the boundary layer mean wind speed to minimize the error in wind field, but there may remain ±20 % uncertainty in the ERA5 reanalysis data. We ran a test by randomly choosing parameter values within their uncertainty ranges for 20 times to predict an ensemble of NO_x and CO_2 emission outcomes. Then the ratio of the standard deviation to the mean value of the 20 emission outcomes is regarded as the uncertainty on NO_x and CO_2 emission caused by uncertainties in the corresponding parameters ~~For each of these factors, we run a test by randomly choosing the data within its uncertainty range for 20 times to estimate NO_x and CO_2 emissions. Then the ratio of the standard deviation to the mean value of the 20 predicted emissions is seen as the uncertainty on NO_x and CO_2 emission caused by corresponding factors~~, which are displayed in Table S2. The uncertainty caused by the domain size is determined by ~~We have~~ narrowing~~ed~~ down our study domain to the Wuhan city center ~~to check the sensitivity of our method to the area of study domain~~ (see Fig. ~~S4~~S7). The results demonstrate that when the study domain is narrowed down to 84 km diameter, and, as expected, the result turns out to be structurally different from that with the 186 km diameter domain, for the mean OH concentration is lower in the city center, leading to longer fitted NO_x lifetime. However, the change in fitted NO_x lifetime and NO_x emission is less than ±15%. So we give an 15% uncertainty in NO_x emission estimation caused by the size in the areas of the study domain. ~~the change in fitted NO_x lifetime and NO_x emission is less than ±15%.~~ Finally, ~~We use the NO_2-column-weighted mean instead of the arithmetic mean value to get the boundary layer mean wind speed to minimize the error in wind field, but there may remain ±20 % uncertainty in the ERA5 reanalysis data.~~ ~~C~~considering that all these parameters are independent from each other, we use the root mean square sum of the

contributions to represent the overall uncertainty estimation, which we quantify for NO_x ~~lifetime and~~ emission on a single day at ~~37~~ 31 %, and for CO_2 emission at ~~48~~ 43 %.

3 Results and discussion

3.1 NO_x Lifetimes and emissions

We display the ~~calculated~~ estimated NO_x lifetime and NO_x emissions for each clear-sky day during the study period in Table ~~S1~~S21. ~~Fitted~~ Estimated planetary boundary layer mean OH concentration over the region for each day is presented in Fig. 2. For 90 % of the days, our model ~~fitted~~ calculated OH concentrations which fall into the intervals of 0.8~1.2× the GEOS-Chem model values. There are only 5 days on which we had to impose a change in OH concentrations of more than 30 % relative to the GEOS-Chem simulation to obtain realistic fitting results.

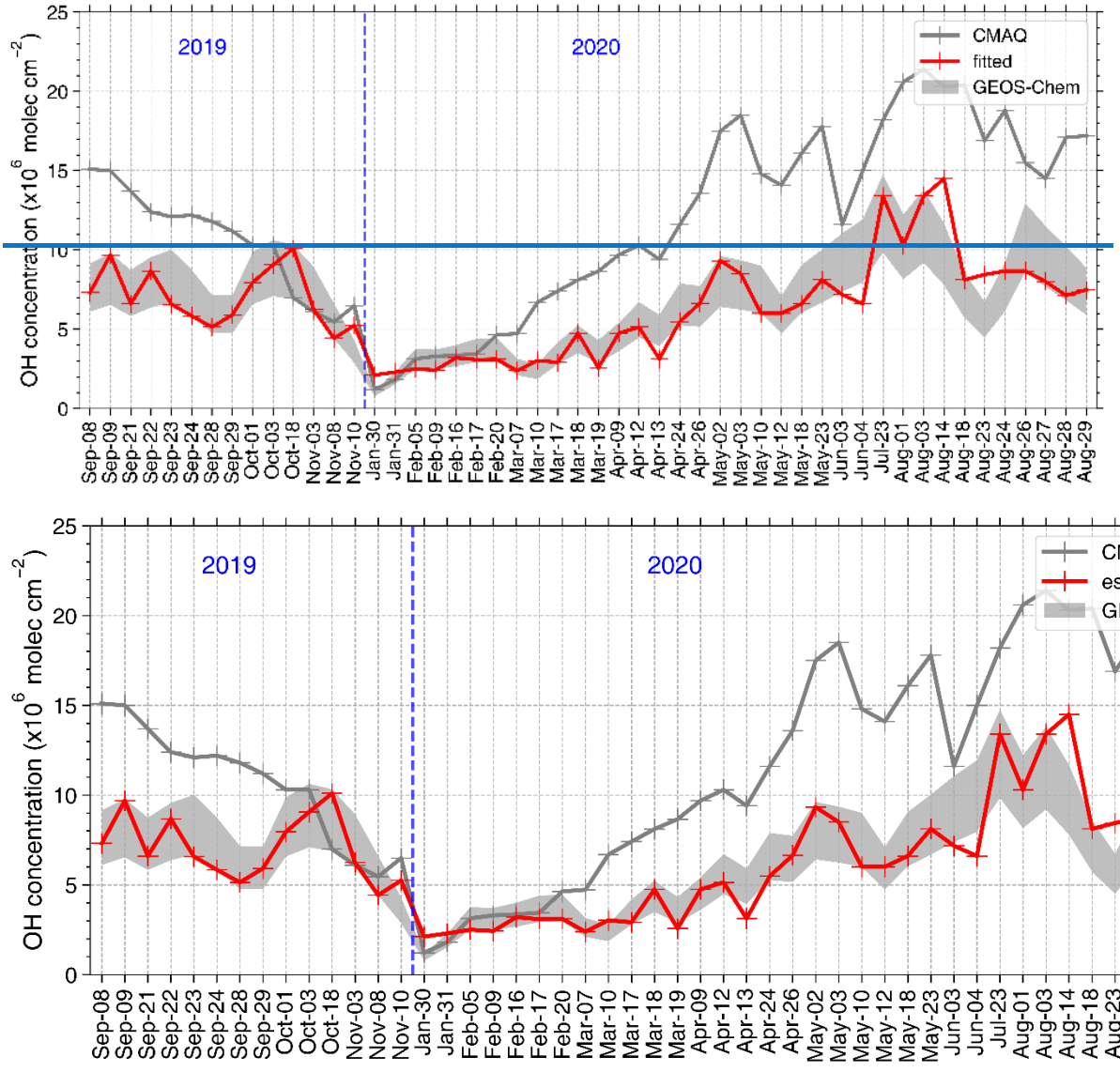

Figure 2: Daily ~~Boundary~~ boundary layer mean OH concentration over our study domain. The OH concentration estimated from our improved superposition column model is given with the red line. The ~~gray~~ grey shade represents 0.8–1.2 times GEOS-Chem simulated OH concentration and the grey line represents CMAQ model simulation results.

We estimate that the seasonal mean noontime NO_x lifetime over Wuhan and adjacent region is 4.8±0.8 h for winter, 2.8±1.3 h for spring, 1.4±0.3 h for summer and 1.9±0.5 h for autumn. The results are lower than those calculated from GEOS-Chem simulation by Shah et al. (2020), with ~6 h in summer and >20 h in winter. This is because they calculated the 24-hour mean NO_x lifetime and the loss rate of NO_x is much higher around noon. NO_x lifetime for Wuhan is also shorter than for Paris

(Lorente et al., 2019), especially during winter, reflecting the higher radiation levels and temperature in Wuhan than in Paris. It should be noted that Liu et al. (2016) fitted a NO_x lifetime of 2.6 h for Wuhan in warm season (May to September) for 2005–2013 mean, and our result for 2019–2020 is 1.7±0.4 h. One reason is that they calculated NO_x lifetimes based on a long-term mean NO_2 distribution, and the coarser resolution of OMI data, both of which lead to spatial smoothing of NO_2 gradients and thus longer apparent NO_x lifetimes (Qu, 2020). Another explanation is the increasing ozone concentrations in China in recent years (Li et al., 2020) which promote OH formation and thereby NO_x loss reactions which shorten NO_x lifetimes (Zara et al., 2021).

The estimated NO_x lifetime and emissions from the two TROPOMI datasets for the whole study period are presented in Fig. S6. On average, the TROPOMI-v1.3 data results in~~generates~~ 13 ~~2.8~~% lower NO_x emissions from Wuhan than the TROPOMI-v2.3.1 data. NO_x lifetime estimated from TROPOMI-v1.3 data is 5 ~~4.9~~% shorter than that from TROPOMI-v2.3.1, which may be attributed to the fact that the TROPOMI-v2.3.1 data has a higher ratio between city center to the background. Uncertainties in NO_x emissions and lifetime estimation (39 %) are also higher in the TROPOMI-v1.3 data (33 %) for the higher uncertainty in the NO_2 column data (here we use 30 %).

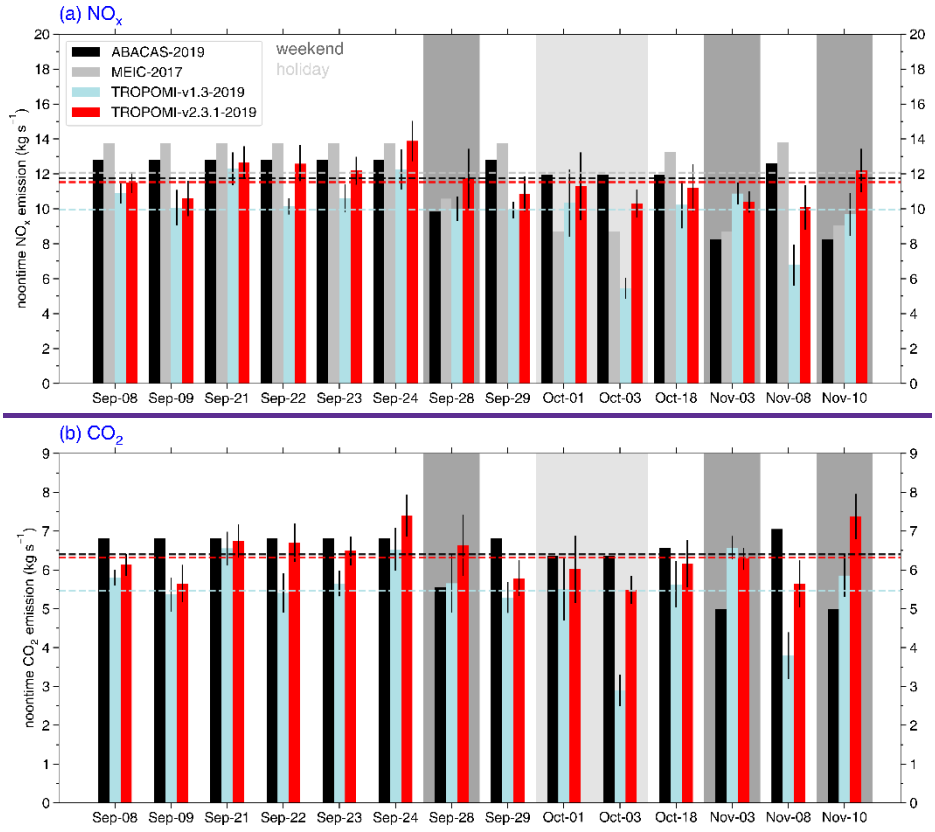
(a) NOx
ABACAS-2019
MEIC-2017
TROPOMI-v1.3-2019
TROPOMI-v2.3.1-2019
weekend
holiday
noontime NOx emission (kg s-1)
(b) CO2
noontime CO2 emission (kg s-1)
Sep-08
Sep-09
Sep-21
Sep-22
Sep-23
Sep-24
Sep-28
Sep-29
Oct-01
Oct-03
Oct-18
Nov-03
Nov-08
Nov-10

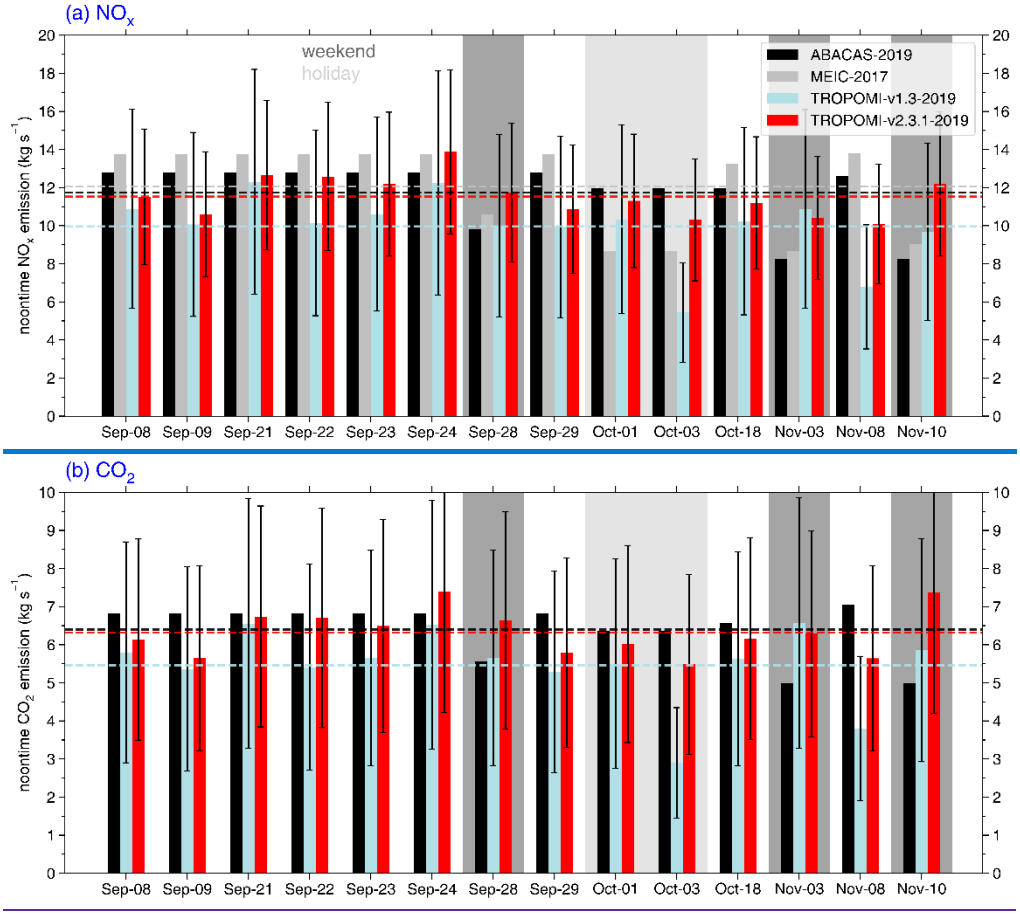
(a) NOx
weekend
holiday
ABACAS-2019
MEIC-2017
TROPOMI-v1.3-2019
TROPOMI-v2.3.1-2019
noontime NOx emission (kg s-1)
Sep-08
Sep-09
Sep-21
Sep-22
Sep-23
Sep-24
Sep-28
Sep-29
Oct-01
Oct-03
Oct-18
Nov-03
Nov-08
Nov-10
(b) CO2
noontime CO2 emission (kg s-1)

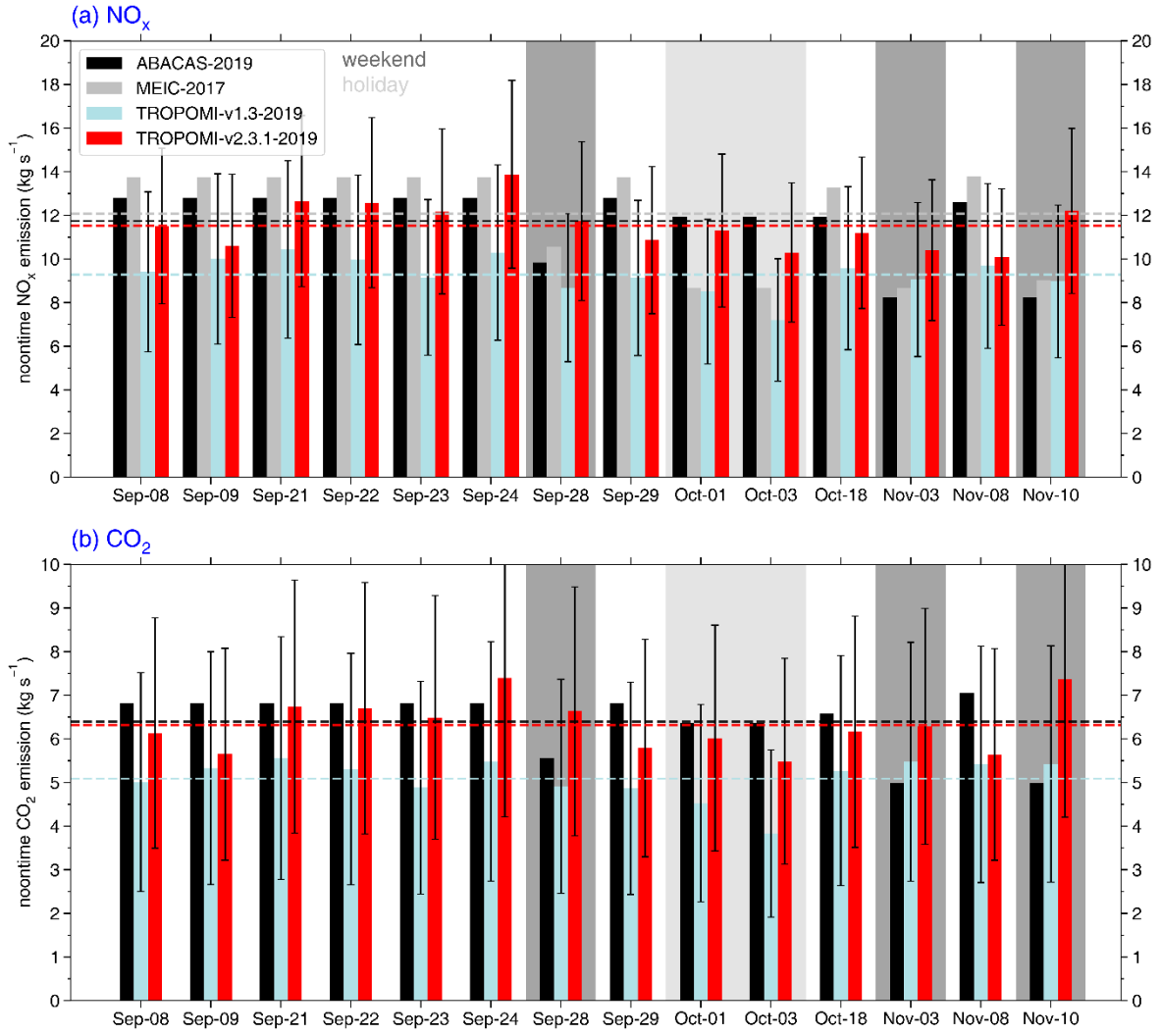

Figure 3: Daily noontime (a) NO_x and (b) CO_2 emissions in Wuhan estimated from TROPOMI (red and blue bars, the error bars represent the ~~standard deviation of the five best estimates for each day~~uncertainty in the emission estimations) and the bottom-up emission inventories ABACAS (black bars) for the year 2019 and MEIC (silver bars) for the year 2017. The dark and light grey shades represent~~s~~ weekends and holidays, respectively. Mean levels of each dataset are given as dashed lines with corresponding colors.

We then further verify the estimated NO_x emissions from the two TROPOMI datasets in 2019 with the bottom-up emission inventories. We obtained ~~The calculated noontime (13:00 local time) NO_x emissions from Wuhan for~~ 14 days (including 9 weekdays, 3 weekends and 2 holidays) between September and November 2019 for the top-down NO_x emission estimation~~,~~ and ~~are compared~~compared them with those from the ABACAS (2019) and MEIC (2017) inventories. Overall, as presented in Fig. 3a, c~~the rescaled TROPOMI-v1.3 estimated noontime NO_x emissions are 13.6% lower than those from TROPOMI-~~

~~v2.3.1. C~~ompared to the bottom-up emission inventories, TROPOMI-v1.3-2019 NO_x emissions are ~~15.120.91~~ % and ~~17.523.13~~ % lower than ABACAS-2019 and MEIC-2017, respectively. On the other hand, TROPOMI-v2.3.1-2019 NO_x emissions are comparable to those from ABACAS-2019 (~~< 3~~1.72 % difference), and ~5 % lower than MEIC-2017. That NO_x emissions estimated from TROPOMI-v2.3.1 in 2019 are lower than MEIC-2017 likely reflects the fact that NO_x emissions have decreased in 2019 relative to 2017 in response to Chinese emission controls. According to Wuhan Bureau of Statistics, NO_x emissions have decreased 6~~.2~~ % between 2017 and 2019 (Statistics, 2019; Bauwens et al., 2020), close to the difference between TROPOMI-v2.3.1-2019 and MEIC-2017. Through the comparison with the bottom-up emissions, we find that the TROPOMI-v2.3.1 NO_2 data generates more reliable NO_x emissions from Wuhan in 2019 than the v1.3 data, even when the low bias in TROPOMI-v1.3 data is corrected by ~~latter is scaled up by~~ a factor of 1.6.

Different to the bottom-up inventories, our daily TROPOMI NO_x emissions do not indicate the existence of a so-called 'weekend reduction effect'~~,~~ but do point out a distinct 'holiday reduction effect' in Wuhan NO_x emissions. The bottom-up inventories suggest that weekend NO_x emissions are 30 % reduced relative to weekdays. The TROPOMI-v2.3.1 estimation shows reductions in weekend NO_x emission of < 3 %, while on the two days (1 and 3 October) of the National Holiday, NO_x emissions are 8% lower than the workday mean. Surface NO_2 and O_3 observations from Beijing do not show a weekend effect (Zhao et al., 2019; Hua et al., 2021) either. Our TROPOMI top-down NO_x emissions show a similar spatial pattern as in the ABACAS and MEIC (Fig. S1), with the highest emissions located in the city center of Wuhan. However, the TROPOMI NO_x emission pattern appears ~~fitted a~~ more smeared-out NO_x ~~emission pattern~~ than ABACAS, due to the strong dependence of the bottom-up spatial distribution on population density, the difference in spatial resolution, and the decrease in NO_x emissions between 2017 and 2020 mainly occurring in the high-emission region.

3.2 CO_2 emissions and XCO_2 enhancements

We estimate noontime top-down (technically representing a ~~it should be a combination~~merger of top-down and bottom-up information, but we define it as top-down for simplicity) CO_2 emissions from Wuhan between September and November 2019 to be 6.32±~~0.60~~2.74 s^{-1} (the errors represent the uncertainty of the emission estimation), comparable to ABACAS-2019, of 6.40±~~0.70~~2.78 t s^{-1} (Fig. 3b). Based on the estimated daily CO_2 emissions, we further use the superposition column model to simulate~~estimate~~ daily XCO_2 ~~enhancements, and~~enhancements and ~~validate~~ evaluate them ~~by~~ with OCO-2 observations. We successfully obtained two days between May 2018 (start time of TROPOMI-v2.3.1 NO_2 product) and December 2021 with simultaneous (both overpass at around 13:00 local time), co-located TROPOMI NO_2 and OCO-2 CO_2 observations over Wuhan: 15 September 2018 and 13 April 2020. We inferred total top-down CO_2 emissions from Wuhan based on our TROPOMI-~~based~~ inferred NO_x emissions and the ABACAS-predicted CO_2-to-NO_x emission ratios on 15 September 2018 and 13 April 2020 to be 7.92±~~0.93~~3.44 t s^{-1} and 4.44±~~0.50~~1.93 t s^{-1} ~~(the errors represent the standard deviation of the 5 best estimations for each day)~~, respectively. We then scaled down the ABACAS 1×1 km^2 gridded CO_2 emissions to match 7.92 t s^{-1} and 4.44 t s^{-1}, and then predict the XCO_2 enhancements using the ~~top-down~~top-down CO_2 emissions in combination with

the superposition column model. It should be noted that to compare with the sparse distributed OCO-2 observations, we apply the superposition model on the CO_2 line density with 1km wide, while it is 186 km wide for NO_2. ~~Since that t~~The column model doesn't take the dispersion of NO_2 or CO_2 into account, but it can be assumed that all dispersion ~~will then be~~is encapsulated within the domain for ~~when~~ a line density ~~covers~~ covering a cross-section as wide as 186 km. However, ~~when the~~for line density is only 1 km wide, the dispersion will move some CO_2 out of this line, and this will influence the CO_2 enhancement prediction. ~~w~~We will discuss ~~its~~ this influence ~~on CO_2 enhancement estimation prediction in the~~ further below.

Neglecting chemical production and loss of CO_2 in the atmosphere, the superposition column model of CO_2 (Eq. 5) is simpler than that of NO_x:

$$N_{CO_2} = \frac{E_{CO_2}}{uL}, \quad (5)$$

Here N_{CO_2} is CO_2 density in unit of g m^{-2}, E_{CO_2} denotes our ~~top down~~estimated CO_2 emission (g s^{-1}), and u and L are the wind speed (m/s) and length of grid cell (6000 m). Then N_{CO_2}(g m^{-2}) is converted to the dry air column mixing ratio XCO_2 (ppm) to compare with the OCO-2 observation (Zheng et al., 2020a):

$$XCO_2 = N_{CO_2} \times \frac{M_{air}}{M_{CO_2}} \times \frac{g}{p - wg} \times 10^3, \quad (6)$$

in which M_{air} and M_{CO_2} are air and CO_2 molar mass of air and CO_2 (g mol^{-1}), g is the gravitational acceleration (9.8 m/s^2), p (Pa) and w (kg m^{-2}) are surface pressure and total column water vapor, respectively.

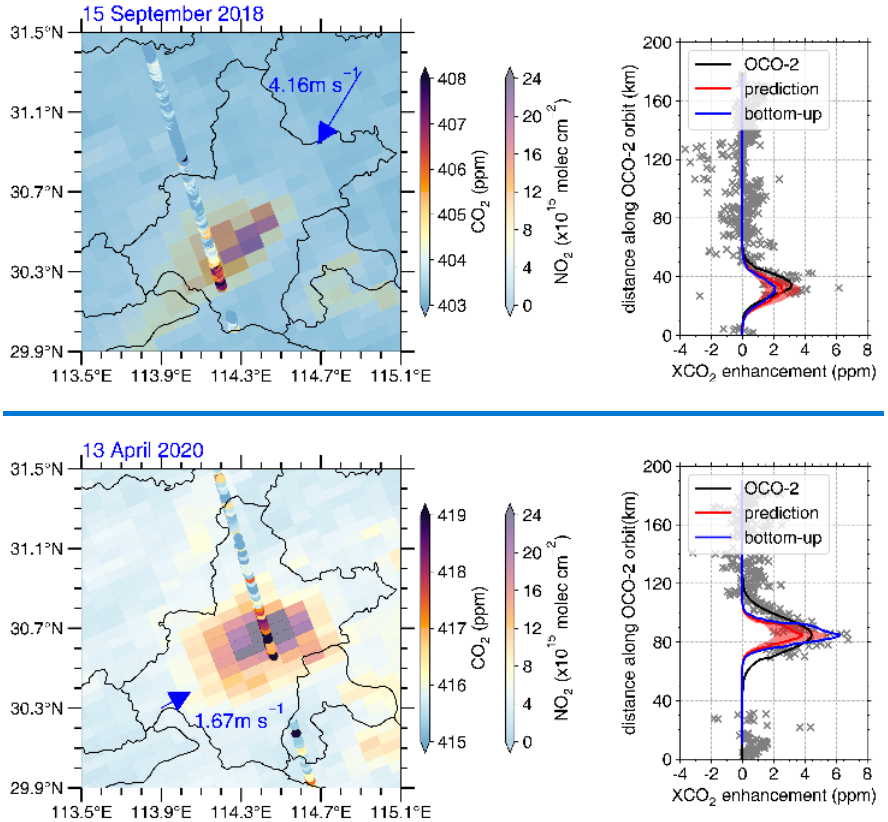
15 September 2018
4.16m s⁻¹
31.5°N
31.1°N
30.7°N
30.3°N
29.9°N
113.5°E
113.9°E
114.3°E
114.7°E
115.1°E
408
407
406
405
404
403
CO2 (ppm)
24
20
16
12
8
4
0
NO2 (x10^15 molec cm^-2)
OCO-2
prediction
bottom-up
distance along OCO-2 orbit (km)
200
160
120
80
40
0
-4
-2
0
2
4
6
8
XCO2 enhancement (ppm)
13 April 2020
1.67m s⁻¹
419
418
417
416
415
CO2 (ppm)
24
20
16
12
8
4
0
NO2 (x10^15 molec cm^-2)
OCO-2
prediction
bottom-up
distance along OCO-2 orbit(km)
XCO2 enhancement (ppm)

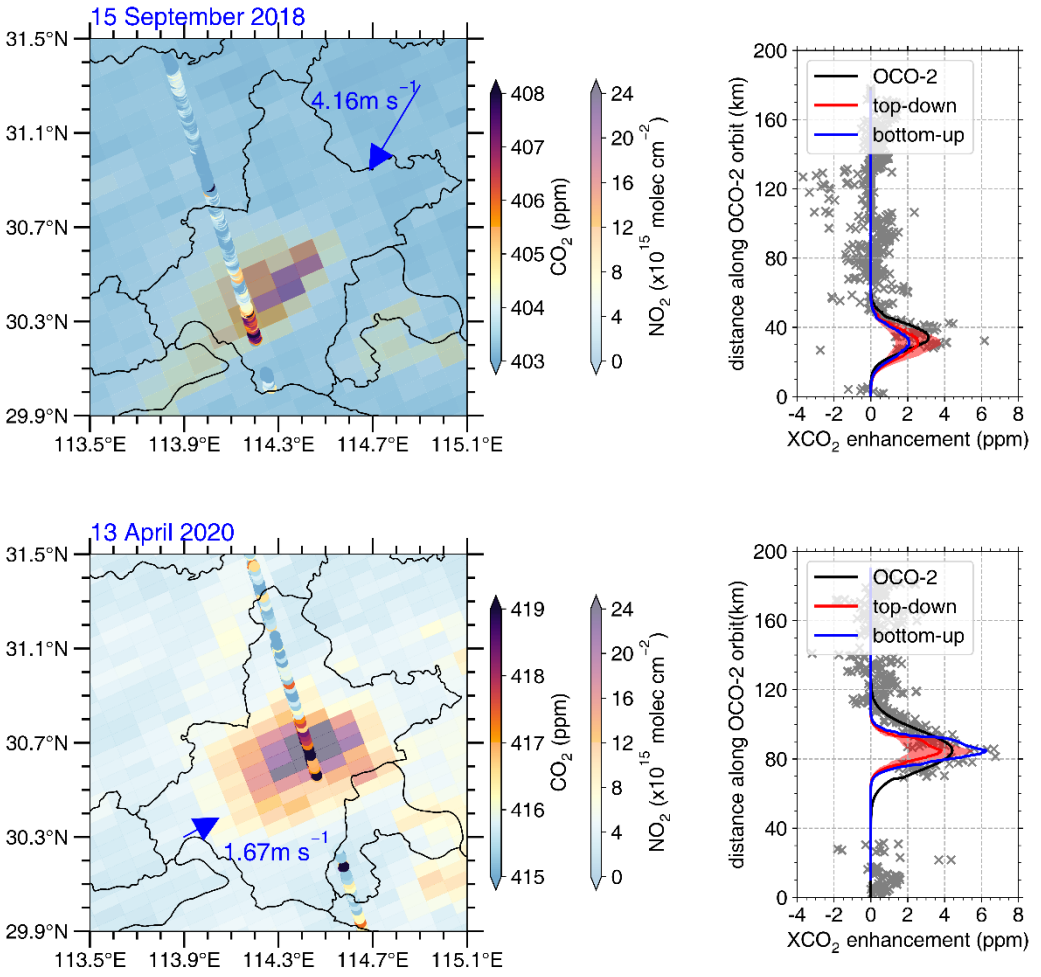

315 **Figure 4: Simultaneous, co-located TROPOMI NO_2 and OCO-2 CO_2 observations over Wuhan (left panel) on 15 September 2018 (top) and 13 April 2020 (bottom), wind speed and direction on each day are shown. The dry air mole fraction of CO_2 (XCO_2) enhancements along the OCO-2 orbit are given for corresponding day (right panel). The gr~~ca~~y xs and black lines represent the OCO-2 observation. The blue lines denote XCO_2 enhancement ~~estimated~~ predicted with bottom-up emissions, and the red lines (shading represents the uncertainty interval) with top-down CO_2 emission ~~predicted~~ estimated in this study.**

320 We calculate the XCO_2 enhancement due ~~our top-down~~to the top-down CO_2 emissions on 15 September 2018 and 13 April 2020 and compare these with the enhancements observed by OCO-2. As shown in the right panels of Fig. 4, the superposition model captures the spatial pattern of observed XCO_2 along the OCO-2 orbit on both days. The predicted amplitudes of the XCO_2 enhancements are also comparable to those in the OCO-2 observation with small bias (less than 5 % for both days). ~~As~~ For comparison, we also use the 2019 bottom-up CO_2 emissions to predict the XCO_2 enhancement on the two days (blue lines 325 in Fig. 4 right panel). XCO_2 enhancements predicted by bottom-up CO_2 emissions deviate more from the OCO-2 observed enhancements than those predicted by ~~our top-down~~the top-down CO_2 emissions. On 13 April 2020 in particular, the bottom-

up enhancement differs by +41% while the top-down differs by only within ±5 % compared to the observed XCO_2 enhancement. At the beginning of Wuhan's reopening, CO_2 emission from the city (our top-down estimation) is expected to be far lower than the pre-lockdown level (bottom-up estimation).

We see that the ~~estimated~~ predicted XCO_2 enhancement on 13 April 2020, both from the bottom-up and top-down emissions, are much 'narrower' compared to the OCO-2 observation. On this day, the OCO-2 orbit passes over the city center and the dispersion plays an important role, which is neglected in the column model. In contrast, on 15 September 2018, the OCO-2 orbit passes downwind of the city center, and the width of the ~~estimated~~ predicted and observed XCO_2 enhancements are more comparable. For comparison, we also ~~conducted~~ ran a Gaussian plume model to ~~estimate~~ simulate the XCO_2 enhancement (Text S4 and Fig. ~~S6~~S8). On 13 April 2020, the result from Gaussian model agrees better with the OCO-2 observation, and on 15 September 2018, results from the two models (Gaussian model and the superposition column model) are close to each other and match well with the observation.

We also display XCO_2 enhancement line densities along wind direction with uncertainty on both days (Fig. 5). The line density shows a substantial increase of XCO_2 along the wind direction over the region with strong CO_2 emissions (Fig.5a, b, the inset maps). Where lines cross the OCO-2 orbit, the observed XCO_2 (as boxplots in Fig. 5a, b) are shown and their values agree with the predicted XCO_2 lines within ±0.3 ppm. It is remarkable that the XCO_2 enhancement is lower on 15 September 2018 than on 13 April 2020, despite CO_2 emissions on 15 September 2018 being nearly 65 % higher than those on 13 April 2020. The main reason for this is the lower wind speed on 13 April 2020, which accumulates pollutants over the city, and the fact that OCO-2 ground-track passed over the city center of Wuhan on this day. On 15 September, higher wind speeds and the OCO-2 track being situated over the outskirts of the city imply that a lower enhancement of CO_2 is observed.

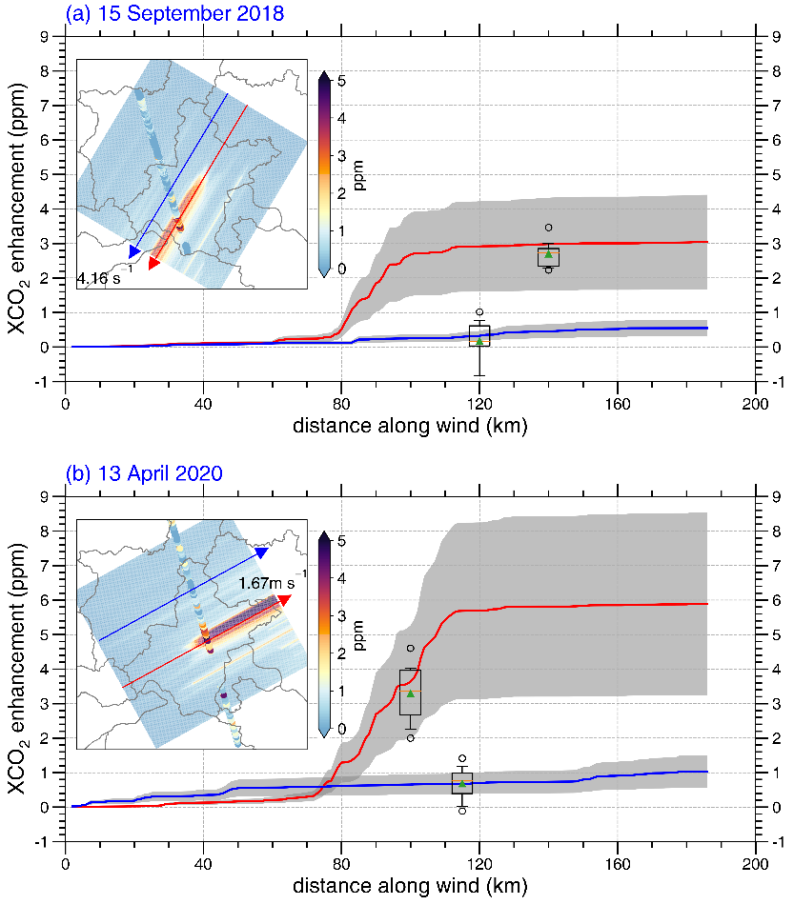

Figure 5: Two presentative predicted XCO_2 enhancement lines (red and blue) with uncertainty (grey shades) on (a) 15 September 2018 and (b) 13 April 2020. When the XCO_2 enhancement line pass through the OCO-2 orbit, the observed XCO_2 enhancements are shown with boxplots, the mean values are shown as green triangles, the outliers beyond the 5–95 % interval are shown as circles. The predicted XCO_2 enhancement line density maps ~~overlayed~~overlaid with OCO-2 observed XCO_2 enhancement on each day are shown inside, with the position of the presentative lines and the wind direction.

We use an 'indirect' method to estimate daily city anthropogenic CO_2 emissions and then predict XCO_2 enhancements, which may in~~tro~~duce uncertainties from the NO_x emission estimation, the assumption of CO_2-to-NO_x emission ratio, and the model to ~~estimate~~ predict XCO_2 enhancements. Despite all these uncertainties, we still generate daily Wuhan CO_2 emissions and XCO_2 enhancements that agree well with bottom-up inventory and OCO-2 observation, respectively.

3.3 Variation of NO_x and CO_2 emissions in Wuhan from September 2019 to August 2020

Figure 6 displays the day-to-day variation of NO_x and CO_2 emissions in Wuhan between September 2019 and August 2020. Before the pandemic of COVID-19, NO_x emissions stay at a stable level of 11.53±1.08 kg s^{-1}, and CO_2 at 6.32±0.66 t s^{-1} (the

errors denote the standard deviation), as indicated by the dashed red lines. From January 2020 onwards, strict lockdown measurements were implemented to combat the COVID-19 pandemic, which led to lower industry production and less traffic on the road, and a sharp drop in NO_x and CO_2 emissions (Ding et al., 2020; Zhang et al., 2020; Zheng et al., 2021b; Zhang et al., 2021; Feng et al., 2020). Our method closely captures the timing and magnitude of these well-known sharp reductions in the emissions.

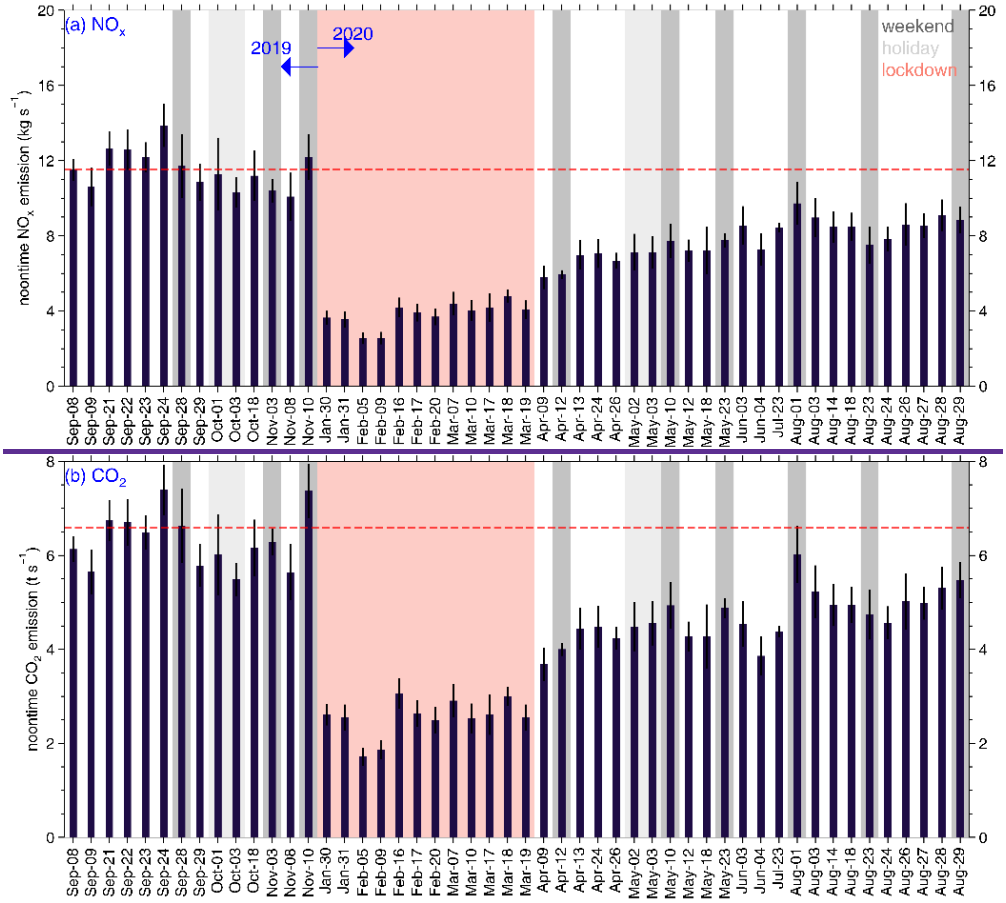
(a) NOx
2019
2020
weekend
holiday
lockdown
noontime NOx emission (kg s-1)
(b) CO2
noontime CO2 emission (t s-1)
Sep-08
Sep-09
Sep-21
Sep-22
Sep-23
Sep-24
Sep-28
Sep-29
Oct-01
Oct-03
Oct-18
Nov-03
Nov-08
Nov-10
Jan-30
Jan-31
Feb-05
Feb-09
Feb-16
Feb-17
Feb-20
Mar-07
Mar-10
Mar-17
Mar-18
Mar-19
Apr-09
Apr-12
Apr-13
Apr-24
Apr-26
May-02
May-03
May-10
May-12
May-18
May-23
Jun-03
Jun-04
Jul-23
Aug-01
Aug-03
Aug-14
Aug-18
Aug-23
Aug-24
Aug-26
Aug-27
Aug-28
Aug-29

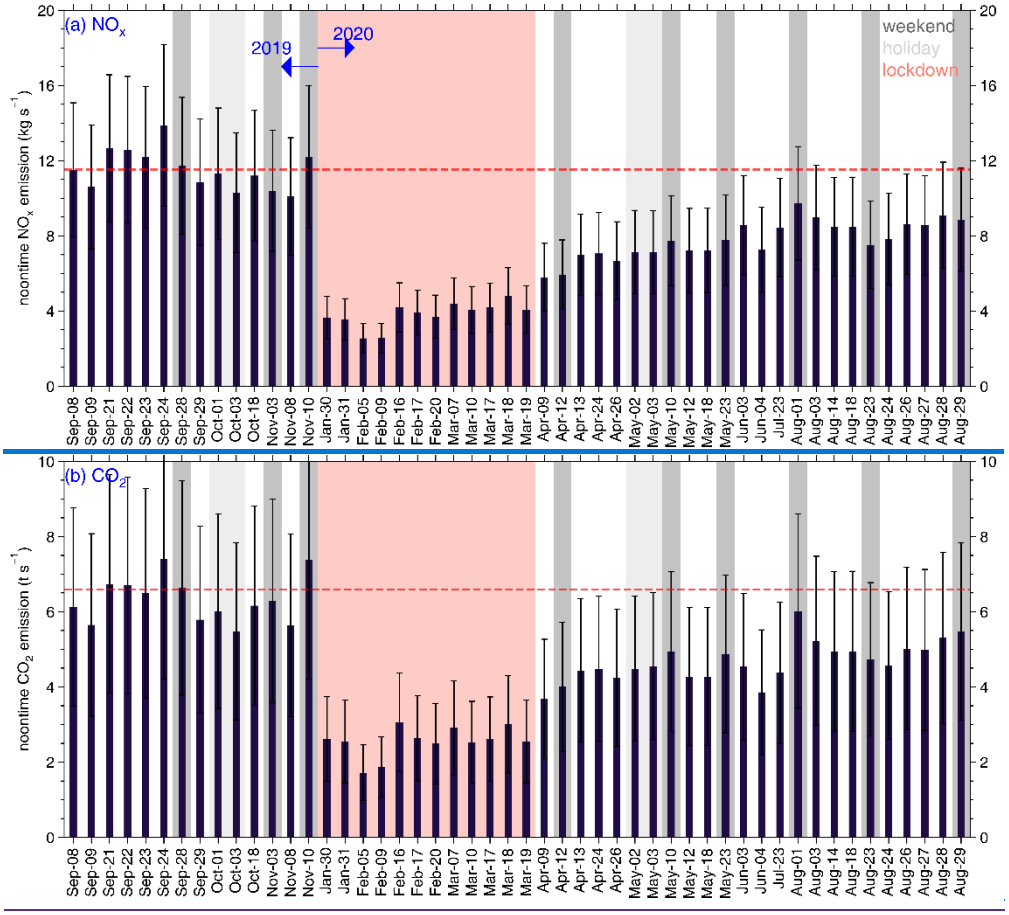
(a) NOx
2019
2020
weekend
holiday
lockdown
noontime NOx emission (kg s-1)
(b) CO2
noontime CO2 emission (t s-1)
Sep-08
Sep-09
Sep-21
Sep-22
Sep-23
Sep-24
Sep-28
Sep-29
Oct-01
Oct-03
Oct-18
Nov-03
Nov-08
Nov-10
Jan-30
Jan-31
Feb-05
Feb-09
Feb-16
Feb-17
Feb-20
Mar-07
Mar-10
Mar-17
Mar-18
Mar-19
Apr-09
Apr-12
Apr-13
Apr-24
Apr-26
May-02
May-03
May-10
May-12
May-18
May-23
Jun-03
Jun-04
Jul-23
Aug-01
Aug-03
Aug-14
Aug-18
Aug-23
Aug-24
Aug-26
Aug-27
Aug-28
Aug-29

365

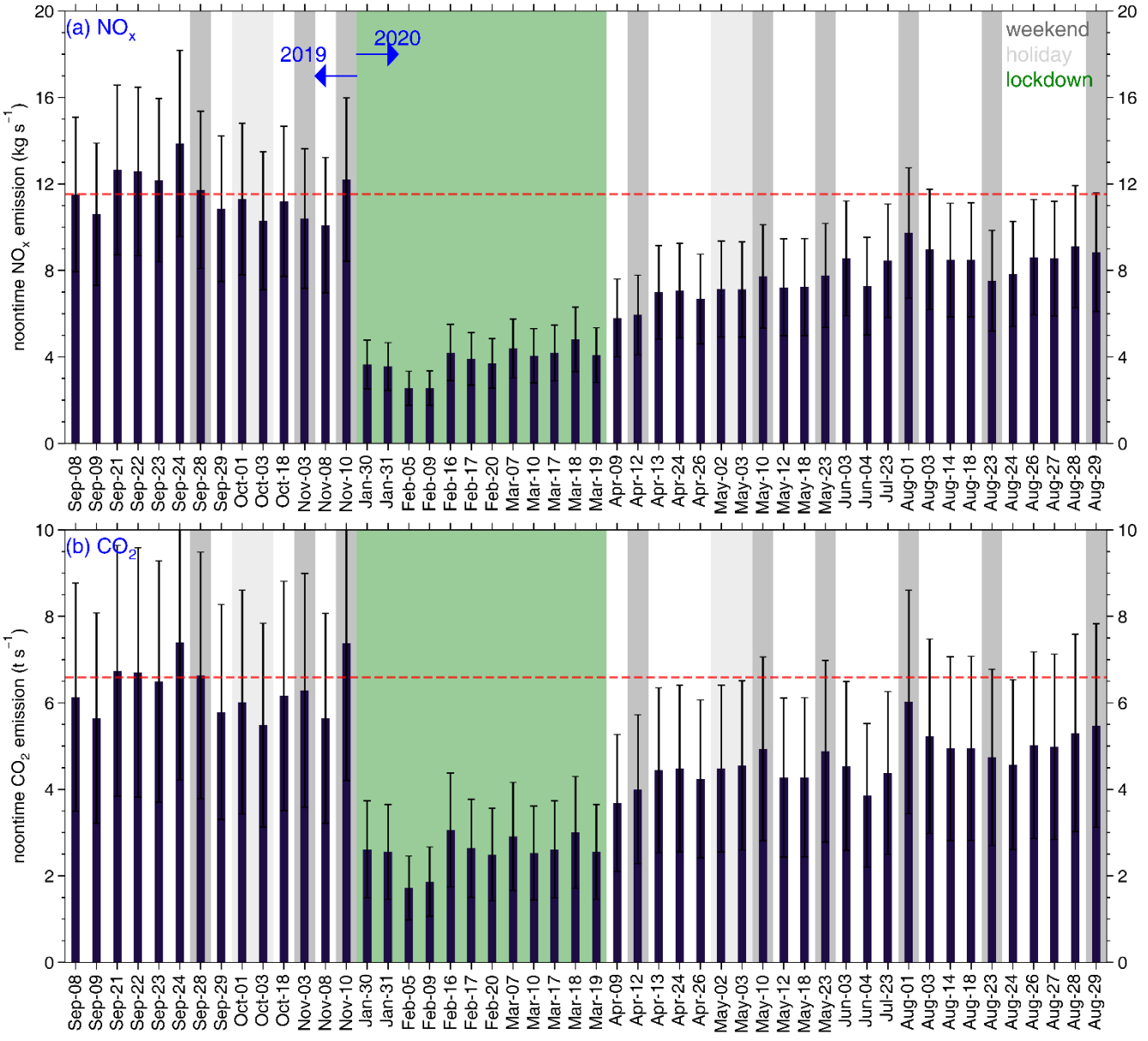

Figure 6: 50 days (a) NO_x and (b) CO_2 emissions in Wuhan estimated from TROPOMI ~~from~~ between 1 September ~~1~~ 2019 to 31 August ~~31~~ 2020. The error bars denote the ~~standard deviation of the five best estimates for each day~~uncertainty in emission estimations, and the weekends, holidays and lockdown period are shaded with dark grey, light grey and green~~red~~ colors, respectively. The mean pre-lockdown emission levels are given as red dashed lines.

Wuhan NO_x emissions on 30 January 2020 are 3.65±~~0.36~~1.59 kg s^{-1}, nearly 70 % lower than pre-lockdown levels, and decreased further and came to the lowest level in early February 2020, in accordance with Feng et al. (2020) who estimated similar reductions based on surface NO_2 observations. 5 February is the day with our lowest NO_x emission from Wuhan of

2.55±~~0.31~~1.11 kg s^{-1}, only ~22 % of the normal level. CO_2 emissions have a similar temporal pattern as NO_x emissions, but the reduction relative to pre-lockdown level is smaller. The lowest CO_2 emission is at ~27 % of the pre-lockdown level (also on 5 February 2020), and the mean emission rate during the lockdown period (23 January to 8 April 2020) is 60 % lower than pre-lockdown level, while it is 67 % for NO_x. That CO_2 emission reductions are more modest than NO_x reductions, reflectings the fact that the transportation sector had the strongest reductions during the lockdown, but since this sector also has the lowest CO_2-to-NO_x ratios, the relative reduction in CO_2 remains somewhat smaller than in NO_x emissions. This finding is similar to that from Zheng et al. (2020b), who estimated the NO_x and CO_2 emission variations for whole China.

From early February 2020 onwards, emissions increased slowly throughout the lockdown period. Wuhan NO_x emission intensity in February 2020 was no more than 4.20 kg s^{-1}, some 60 % below the pre-lockdown level. Feng et al. (2020) estimated 61 % lower NO_x emission from Wuhan in February 2020 than January based on surface NO_x observations. Zheng et al. (2021a) reported a ~50 % lower NO_x emission from Hubei in February 2020 than the annual mean level estimated from a bottom-up approach.

Although Wuhan reopened on 9 April, the NO_x and CO_2 emissions didn't see significant increases up until mid-May 2020. A perceptible increase in NO_x emission is seen during late May, climbing to > 7.50 kg s^{-1} (NO_x) and > 4.5 t s^{-1} (CO_2), and levelling off thereafter. In August 2020, Wuhan NO_x emissions were still some 25 % lower than the pre-lockdown level. Although bottom-up estimation by Zheng et al. (2021a) suggested that NO_x emissions from the Hubei province were similar in May–August 2020 as in 2019, surface and satellite observations over Wuhan show a 15–20 % lower NO_2 concentrations in May–August 2020 compared to 2019 (Fig. ~~S7~~ S9 and ~~S8~~S10), consistent with our estimation of NO_x emission. Liu et al. (2020c) reported 4.8 % higher CO_2 emissions for the whole China in August 2020 compared to August 2019. For the city of Wuhan, however, we calculate here some 20 % lower CO_2 emissions in August 2020 compared to the pre-lockdown level. Wuhan experienced a much more strict and longer period lockdown than other regions of China, and therefore a slower rebound of NO_x and CO_2 emissions should be expected over Wuhan.

As we have stated above, to assure the performance of the model, we must filter out the days when cloud fraction is greater than 0.2 and the days when the wind direction shows substantial spatial or temporal variation within the study domain. Finally, we obtain 50 out of the 365 days with reliable NO_x and CO_2 emissions estimation. However, these 50 days covers at least 2 days for each month (except for December 2019). For 2019, it includes 9 workdays, 3 weekend days and 2 holiday days, which are enough to investigate the 'weekend ~~effect~~reduction effect' and 'holiday reduction effect~~effect~~' in NO_x emissions. It also covers 12 days across the lockdown period and 24 days after that, allowing us to monitor the large reduction and recover of NO_x and CO_2 from Wuhan due to the COVID lockdown. Therefore, these 50 days provide useful information to investigate the temporal emission patterns of NO_x and CO_2 from Wuhan and help to monitor the effectiveness of emission reductions in large urban centers.

4 Conclusion

In this study, we introduced an improved superposition column model to estimate daily NO_x and CO_2 emissions from a Chinese megacity of Wuhan based on the latest released version 2.3.1 of TROPOMI NO_2 column data and OCO-2 XCO_2 observation. Our estimated daily NO_x and CO_2 emissions agree well with bottom-up emissions with small bias of < 3 %. Predicted XCO_2 enhancements based on our CO_2 emissions estimates prove to be in good agreement (within ±5 %) with OCO-2 observations over Wuhan. Compared to previous studies, our work shows that satellite measurements can provide detailed information on sub-city -scale NO_x and CO_2 emissions ~~at unprecedented spatial and temporal resolutions~~on daily basis. We achieved the day-to-day variation of NO_x and CO_2 emissions from Wuhan between September 2019 and August 2020. We pointed out that the 'weekend reduction effect' is small, but that a 'holiday reduction effect' in Wuhan NO_x and CO_2 emissions can be clearly detected. We also captured the abrupt decrease in NO_x and CO_2 emissions as the lockdown for COVID began on 23 January 2020, and the slow rebound as Wuhan reopened on 9 April 2020. Daily updates of city-scale NO_x and CO_2 emissions provides policy makers with emission and policy control data on NO_x and CO_2 emission control in urban environments.

In the future, following the launch of the Carbon Dioxide Monitoring mission (CO2M) (Sierk et al., 2021), our improved superposition column method may be explored further to constrain city scale CO_2 and NO_x emissions to assess the effectiveness of emission control measures. CO2M provides simultaneous and co-located CO_2 and NO_2 observations with a wider swath than OCO-2, providing better opportunities to verify and improve CO_2 and NO_x emissions from space.

.

Data availability. The S-5P TROPOMI v2.3.1 NO2 column data is available from https://data-portal.s5p-pal.com/cat-doc (last access: 3, November 2022); the ERA5 data can be found at https://cds.climate.copernicus.eu/cdsapp#!/dataset/reanalysis-era5-pressure-levels?tab=overview (last access: 3, November 2022); the OCO-2 v10r XCO_2 data can be downloaded from (last access: 3, November 2022); The GEOS-Chem model simulated data is available on request (zhangqq@cma.gov.cn).

Author contributions. Q.Z. and K.F.B designed the research; Q.Z. performed the data analysis, model development and result validation. B.Z. and H.Z. provide the ABACAS-EI NO_x and CO_2 emission inventories. H.E. provides the 2.3.1 version of TROPOMI tropospheric NO_2 product. C.C. provides MEIC NO_x emissions and perform the CMAQ simulations. X. Z. provided helpful discussions. Q.Z. and K.F.B. wrote the paper.

Competing interests. The authors declare no competing financial interest.

Acknowledgement. This work is funded by the National Natural Science Foundation of China (No.: 41805098) and the China Scholarship Council (202005330023). Improvements in TROPOMI NO_2 data (v2.3.1) have received support from the KNMI MSO NO_2NEXT project.

References

Bauwens, M., Compernolle, S., Stavrakou, T., Muller, J. F., van Gent, J., Eskes, H., Levelt, P. F., van der, A. R., Veefkind, J. P., Vlietinck, J., Yu, H., and Zehner, C.: Impact of coronavirus outbreak on NO_2 pollution assessed using TROPOMI and OMI observations, Geophys. Res. Lett., e2020GL087978, 10.1029/2020GL087978, 2020.

Beirle, S., Boersma, K. F., Platt, U., Lawrence, M. G., and Wagner, T.: Megacity emissions and lifetimes of nitrogen oxides probed from space, Science, 333, 1737-1739, 10.1126/science.1207824, 2011.

Beirle, S. B., K.F., Platt, U., Lawrence, M.G., Wagner, T.: Megacity Emissions and Lifetimes of Nitrogen Oxides Probed from Space, Science, 333, 2011.

Berezin, E. V., Konovalov, I. B., Ciais, P., Richter, A., Tao, S., Janssens-Maenhout, G., Beekmann, M., and Schulze, E. D.: Multiannual changes of CO_2 emissions in China: indirect estimates derived from satellite measurements of tropospheric NO_2 columns, Atmos. Chem. Phys., 13, 9415-9438, 10.5194/acp-13-9415-2013, 2013.

Ding, J., A, R. J., Eskes, H. J., Mijling, B., Stavrakou, T., Geffen, J. H. G. M., and Veefkind, J. P.: NO_x Emissions Reduction and Rebound in China Due to the COVID-19 Crisis, Geophys. Res. Lett., 47, 10.1029/2020gl089912, 2020.

Eskes, H., Van Geffen, J., Sneep, M., Veefkind, J. P., Niemeijer, S., and Zehner, C.: S5P Nitrogen Dioxide v02.03.01 intermediate reprocessing on the S5P-PAL system: Readme file, 2021.

Feng, S., Jiang, F., Wang, H., Wang, H., Ju, W., Shen, Y., Zheng, Y., Wu, Z., and Ding, A.: NO_x Emission Changes Over China During the COVID-19 Epidemic Inferred From Surface NO_2 Observations, Geophys. Res. Lett., 47, e2020GL090080, 10.1029/2020GL090080, 2020.

Griffin, D., McLinden, C. A., Boersma, F., Bourassa, A., Dammers, E., Degenstein, D., Eskes, H., Fehr, L., Fioletov, V., Hayden, K., Kharol, S. K., Li, S. M., Makar, P., Martin, R. V., Mihele, C., Mittermeier, R. L., Krotkov, N., Sneep, M., Lamsal, L. N., Ter Linden, M., van Geffen, J., Veefkind, P., Wolde, M., and Zhao, X.: High resolution mapping of nitrogen dioxide with TROPOMI: First results and validation over the Canadian oil sands, Geophys. Res. Lett., 46, 1049-1060, 10.1029/2018GL081095, 2019.

Gunson M and Eldering, A.: OCO-2 Level 2 bias-corrected XCO_2 and other select fields from the full-physics retrieval aggregated as daily files, Retrospective processing V10r, Greenbelt, MD, USA, Goddard Earth Sciences Data and Information Services Center (GES DISC), last access: 31-05-2022, 10.5067/E4E140XDMPO2, 2020.

Hersbach, H., Bell, B., Berrisford, P., Hirahara, S., Horányi, A., Muñoz-Sabater, J., Nicolas, J., Peubey, C., Radu, R., Schepers, D., Simmons, A., Soci, C., Abdalla, S., Abellan, X., Balsamo, G., Bechtold, P., Biavati, G., Bidlot, J., Bonavita, M., Chiara, G., Dahlgren, P., Dee, D., Diamantakis, M., Dragani, R., Flemming, J., Forbes, R., Fuentes, M., Geer, A., Haimberger, L., Healy, S., Hogan, R. J., Hólm, E., Janisková, M., Keeley, S., Laloyaux, P., Lopez, P., Lupu, C., Radnoti, G., Rosnay, P., Rozum, I., Vamborg, F., Villaume, S., and Thépaut, J. N.: The ERA5 global reanalysis, Q J R Meteorol Soc., 146, 1999-2049, 10.1002/qj.3803, 2020.

Hua, J., Zhang, Y., de Foy, B., Mei, X., Shang, J., and Feng, C.: Competing $PM_{2.5}$ and NO_2 holiday effects in the Beijing area vary locally due to differences in residential coal burning and traffic patterns, Sci. Total. Environ., 750, 141575, 10.1016/j.scitotenv.2020.141575, 2021.

Huang, X., Ding, A., Gao, J., Zheng, B., Zhou, D., Qi, X., Tang, R., Wang, J., Ren, C., Nie, W., Chi, X., Xu, Z., Chen, L., Li, Y., Che, F., Pang, N., Wang, H., Tong, D., Qin, W., Cheng, W., Liu, W., Fu, Q., Liu, B., Chai, F., Davis, S. J., Zhang, Q., and He, K.: Enhanced secondary pollution offset reduction of primary emissions during COVID-19 lockdown in China, Natl Sci Rev., 8, nwaa137, 10.1093/nsr/nwaa137, 2021.

Jacob, D.: Introduction to Atmospheric Chemistry, Princeton Univ. Press, 1999.

Lamsal, L. N., Martin, R. V., Padmanabhan, A., van Donkelaar, A., Zhang, Q., Sioris, C. E., Chance, K., Kurosu, T. P., and Newchurch, M. J.: Application of satellite observations for timely updates to global anthropogenic NO_x emission inventories, Geophys. Res. Lett., 38, n/a, 10.1029/2010gl046476, 2011.

Lamsal, L. N., Martin, R. V., van Donkelaar, A., Celarier, E. A., Bucsela, E. J., Boersma, K. F., Dirksen, R., Luo, C., and Wang, Y.: Indirect validation of tropospheric nitrogen dioxide retrieved from the OMI satellite instrument: Insight into the seasonal variation of nitrogen oxides at northern midlatitudes, J. Geophys. Res., 115, 10.1029/2009jd013351, 2010.

Li, K., Jacob, D. J., Shen, L., Lu, X., De Smedt, I., and Liao, H.: Increases in surface ozone pollution in China from 2013 to 2019: anthropogenic and meteorological influences, Atmos. Chem. Phys., 20, 11423-11433, 10.5194/acp-20-11423-2020, 2020.

Li, M., Zhang, Q., Kurokawa, J.-i., Woo, J.-H., He, K., Lu, Z., Ohara, T., Song, Y., Streets, D. G., Carmichael, G. R., Cheng, Y., Hong, C., Huo, H., Jiang, X., Kang, S., Liu, F., Su, H., and Zheng, B.: MIX: a mosaic Asian anthropogenic emission inventory under the international collaboration framework of the MICS-Asia and HTAP, Atmos. Chem. Phys., 17, 935-963, 10.5194/acp-17-935-2017, 2017.

Liu, F., Beirle, S., Zhang, Q., Dörner, S., He, K., and Wagner, T.: NO_x lifetimes and emissions of cities and power plants in polluted background estimated by satellite observations, Atmos. Chem. Phys., 16, 5283-5298, 10.5194/acp-16-5283-2016, 2016.

Liu, F., Duncan, B. N., Krotkov, N. A., Lamsal, L. N., Beirle, S., Griffin, D., McLinden, C. A., Goldberg, D. L., and Lu, Z.: A methodology to constrain carbon dioxide emissions from coal-fired power plants using satellite observations of co-emitted nitrogen dioxide, Atmos. Chem. Phys., 20, 99-116, 10.5194/acp-20-99-2020, 2020a.

Liu, M., Lin, J., Kong, H., Boersma, K. F., Eskes, H., Kanaya, Y., He, Q., Tian, X., Qin, K., Xie, P., Spurr, R., Ni, R., Yan, Y., Weng, H., and Wang, J.: A new TROPOMI product for tropospheric NO_x columns over East Asia with explicit aerosol corrections, Atmos. Meas. Tech., 13, 4247-4259, 10.5194/amt-13-4247-2020, 2020b.

Liu, Z., Ciais, P., Deng, Z., Davis, S. J., Zheng, B., Wang, Y., Cui, D., Zhu, B., Dou, X., Ke, P., Sun, T., Guo, R., Zhong, H., Boucher, O., Breon, F. M., Lu, C., Guo, R., Xue, J., Boucher, E., Tanaka, K., and Chevallier, F.: Carbon Monitor, a near-real-time daily dataset of global CO_2 emission from fossil fuel and cement production, Sci. Data, 7, 392, 10.1038/s41597-020-00708-7, 2020c.

Lorente, A., Boersma, K. F., Eskes, H. J., Veefkind, J. P., van Geffen, J., de Zeeuw, M. B., Denier van der Gon, H. A. C., Beirle, S., and Krol, M. C.: Quantification of nitrogen oxides emissions from build-up of pollution over Paris with TROPOMI, Sci. Rep., 9, 20033, 10.1038/s41598-019-56428-5, 2019.

ODell, C., Eldering, A., Gunson , M., Crisp, D., Fisher, B., Kiel, M., Kuai, L., Laughner, J., Merrelli, A., Nelson, R., Osterman, G., Payne, V., Rosenberg, R., Taylor, T., Wennberg, P., Kulawik, S., Lindqvist, H., Miller, S., and Nassar, R.: Improvements in XCO_2 accuracy from OCO-2 with the latest ACOS v10 product, EGU General Assembly 2021, online, 19–30 Apr 2021, EGU21-10484, 2021.

Qu, H.: Summertime ozone pollution over China: observations and simulations, Dissertation for the degree of Doctor of Philosophy, School of Earth and Atmospheric Science, Georfia Institute of Technology, 2020.

Reuter, M., Buchwitz, M., Schneising, O., Krautwurst, S., O'Dell, C. W., Richter, A., Bovensmann, H., and Burrows, J. P.: Towards monitoring localized CO_2 emissions from space: co-located regional CO_2 and NO_2 enhancements observed by the OCO-2 and S5P satellites, Atmos. Chem. Phys., 19, 9371-9383, 10.5194/acp-19-9371-2019, 2019.

Reuter, M., Buchwitz, M., Hilboll, A., Richter, A., Schneising, O., Hilker, M., Heymann, J., Bovensmann, H., and Burrows, J. P.: Decreasing emissions of NO_x relative to CO_2 in East Asia inferred from satellite observations, Nature Geosci., 7, 792-795, 10.1038/ngeo2257, 2014.

Riess, T. C. V. W., Boersma, K. F., van Vliet, J., Peters, W., Sneep, M., Eskes, H., and van Geffen, J.: Improved monitoring of shipping NO_2 with TROPOMI: decreasing NO_x emissions in European seas during the COVID-19 pandemic, Atmos. Meas. Tech., 15, 1415-1438, 10.5194/amt-15-1415-2022, 2022.

Shah, V., Jacob, D. J., Li, K., Silvern, R. F., Zhai, S., Liu, M., Lin, J., and Zhang, Q.: Effect of changing NO_x lifetime on the seasonality and long-term trends of satellite-observed tropospheric NO_2 columns over China, Atmos. Chem. and Phys., 20, 1483-1495, 10.5194/acp-20-1483-2020, 2020.

Sierk, B., Fernandez, V., Bézy, J. L., Meijer, Y., Durand, Y., Bazalgette Courrèges-Lacoste, G., Pachot, C., Löscher, A., Nett, H., Minoglou, K., Boucher, L., Windpassinger, R., Pasquet, A., Serre, D., te Hennepe, F., Sodnik, Z., Cugny, B., and Karafolas, N.: The Copernicus CO2M mission for monitoring anthropogenic carbon dioxide emissions from space, International Conference on Space Optics — ICSO 2020, 10.1117/12.2599613, 2021.

Statistics, W. B. o.: Statistical Bulletin on domestic economic and social development of Wuhan (2018), http://tjj.wuhan.gov.cn/tjfw/tjgb/202001/t20200115_841065.shtml (in Chinese, last access: 2022-05-19), 2019.

van Geffen, J., Boersma, K. F., Eskes, H., Sneep, M., ter Linden, M., Zara, M., and Veefkind, J. P.: S5P TROPOMI NO_2 slant column retrieval: method, stability, uncertainties and comparisons with OMI, Atmos. Meas. Tech., 13, 1315-1335, 10.5194/amt-13-1315-2020, 2020.

van Geffen, J., Eskes, H., Compernolle, S., Pinardi, G., Verhoelst, T., Lambert, J.-C., Sneep, M., ter Linden, M., Ludewig, A., Boersma, K. F., and Veefkind, J. P.: Sentinel-5P TROPOMI NO_2 retrieval: impact of version v2.2 improvements and comparisons with OMI and ground-based data, Atmos. Meas. Tech., 15, 2037-2060, 10.5194/amt-15-2037-2022, 2022.

Visser, A. J., Boersma, K. F., Ganzeveld, L. N., and Krol, M. C.: European NO_x emissions in WRF-Chem derived from OMI: impacts on summertime surface ozone, Atmos. Chem. Phys., 19, 11821-11841, 10.5194/acp-19-11821-2019, 2019.

Wang, C., Wang, T., Wang, P., and Rakitin, V.: Comparison and Validation of TROPOMI and OMI NO2 Observations over China, Atmosphere, 11, 10.3390/atmos11060636, 2020.

Zara, M., Boersma, K. F., Eskes, H., Denier van der Gon, H., Vilà-Guerau de Arellano, J., Krol, M., van der Swaluw, E., Schuch, W., and Velders, G. J. M.: Reductions in nitrogen oxides over the Netherlands between 2005 and 2018 observed from space and on the ground: Decreasing emissions and increasing O_3 indicate changing NO_x chemistry, Atmos. Environ.: X, 9, 10.1016/j.aeaoa.2021.100104, 2021.

Zhang, Q., Pan, Y., He, Y., Walters, W. W., Ni, Q., Liu, X., Xu, G., Shao, J., and Jiang, C.: Substantial nitrogen oxides emission reduction from China due to COVID-19 and its impact on surface ozone and aerosol pollution, Sci. Total. Environ., 753, 142238, 10.1016/j.scitotenv.2020.142238, 2021.

Zhang, R., Zhang, Y., Lin, H., Feng, X., Fu, T.-M., and Wang, Y.: NO_x Emission Reduction and Recovery during COVID-19 in East China, Atmosphere, 11, 10.3390/atmos11040433, 2020.

Zhao, B., Wang, S. X., Liu, H., Xu, J. Y., Fu, K., Klimont, Z., Hao, J. M., He, K. B., Cofala, J., and Amann, M.: NO_x emissions in China: historical trends and future perspectives, Atmos. Chem. Phys., 13, 9869-9897, 10.5194/acp-13-9869-2013, 2013.

Zhao, B., Zheng, H., Wang, S., Smith, K. R., Lu, X., Aunan, K., Gu, Y., Wang, Y., Ding, D., Xing, J., Fu, X., Yang, X., Liou, K. N., and Hao, J.: Change in household fuels dominates the decrease in $PM_{2.5}$ exposure and premature mortality in China in 2005-2015, Proc. Natl. Acad. Sci. USA, 115, 12401-12406, 10.1073/pnas.1812955115, 2018.

Zhao, X., Zhou, W., and Han, L.: Human activities and urban air pollution in Chinese mega city: An insight of ozone weekend effect in Beijing, Phys. Chem. Earth, 110, 109-116, 10.1016/j.pce.2018.11.005, 2019.

Zheng, B., Zhang, Q., Geng, G., Shi, Q., Lei, Y., and He, K.: Changes in China's anthropogenic emissions during the COVID-19 pandemic [data set], figshare, Collection, https://doi.org/10.6084/m9.figshare.c.5214920.v2, 2021a.

Zheng, B., Chevallier, F., Ciais, P., Broquet, G., Wang, Y., Lian, J., and Zhao, Y.: Observing carbon dioxide emissions over China's cities and industrial areas with the Orbiting Carbon Observatory-2, Atmos. Chem. Phys., 20, 8501-8510, 10.5194/acp-20-8501-2020, 2020a.

Zheng, B., Zhang, Q., Geng, G., Chen, C., Shi, Q., Cui, M., Lei, Y., and He, K.: Changes in China's anthropogenic emissions and air quality during the COVID-19 pandemic in 2020, Earth Syst. Sci. Data, 13, 2895-2907, 10.5194/essd-13-2895-2021, 2021b.

Zheng, B., Geng, G., Ciais, P., Davis, S. J., Martin, R. V., Meng, J., Wu, N., Chevallier, F., Broquet, G., Boersma, F., van der A, R. J., Lin, J., Guan, D., Lei, Y., He, K., and Zhang, Q.: Satelite-based estimats of decline and rebound in China's CO_2 emissions during COVID-19 pandemic, Sci. Adv., 6, eabd4998, 2020b.

Zheng, B., Geng, G., Ciais, P., Davis, S. J., Martin, R. V., Meng, J., Wu, N., Chevallier, F., Broquet, G., Boersma, F., van der, A. R., Lin, J., Guan, D., Lei, Y., He, K., and Zhang, Q.: Satellite-based estimates of decline and rebound in China's CO_2 emissions during COVID-19 pandemic, Sci. Adv., 6, 10.1126/sciadv.abd4998, 2020c.

Zheng, H., Zhao, B., Wang, S., Wang, T., Ding, D., Chang, X., Liu, K., Xing, J., Dong, Z., Aunan, K., Liu, T., Wu, X., Zhang, S., and Wu, Y.: Transition in source contributions of $PM_{2.5}$ exposure and associated premature mortality in China during 2005-2015, Environ. Int., 132, 105111, 10.1016/j.envint.2019.105111, 2019.

SUPPLEMENTARY FOR

Quantifying daily NO_x and CO_2 emissions from Wuhan using satellite observations from TROPOMI and OCO-2

Qianqian Zhang[1,2], K. Folkert Boersma[1,3], Bin Zhao[4], Henk Eskes[3], Cuihong Chen[5], Haotian Zheng[4], Xingying Zhang[2]

[1] Wageningen University, Environmental Science Group, Wageningen, the Netherlands

[2] Key Laboratory of Radiometric Calibration and Validation for Environmental Satellites, Innovation Center for Fengyun Meteorological Satellite (FYSIC), National Satellite Meteorological Center, China Meteorology Administration, Beijing, 100081, China

[3] Royal Netherlands Meteorological Institute, De Bilt, the Netherlands

[4] State Key Joint Laboratory of Environmental Simulation and Pollution Control, School of environment, Tsinghua University, Beijing 100084, China

[5] Satellite Application Center for Ecology and Environment, Ministry of Ecology and Environment of the People's Republic of China, Beijing, 100094, China

Correspondence to: K. Folkert Boersma, folkert.boersma@wur.nl, Qianqian Zhang, zhangqq@cma.gov.cn

1. Emission spatial patterns

In the process of fitting the NO_x emissions from Wuhan, we give a first guess of spatial pattern of NO_x emission, i.e. the spatial pattern from the MEIC-2017 and ABACAS-2017 bottom-up inventories (~~-~~blue and black lines in Fig. S1). To be mentioned, the top-down NO_x emission pattern is smoother compared to the bottom-up emissions. This is caused by two reasons. First, the spatial resolution of the bottom-up emission inventories are 1 km × 1 km, while it is 5 km × 5 km for ~~each particular day,~~the top-down emissions. Second, the spatial pattern of the bottom-up emission inventories is used as a first guess for the predicted emissions, but we let it shift along with the wind ~~direction~~during the fitting, and ~~finally obtain~~ the ~~fitted~~final predicted NO_x emission ~~spatial~~ pattern ~~(red line in Fig. S1).~~is determined by the mean of all the valid days.

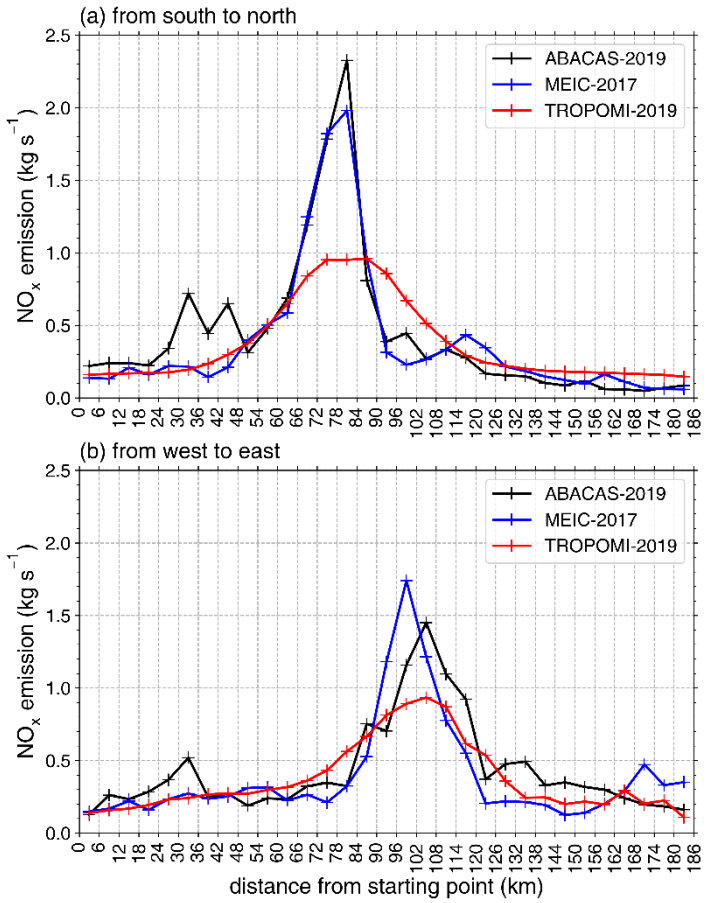

Figure S1: Spatial pattern of NO_x emissions in Wuhan from ABACAS-EI, MEIC and our fitted results.

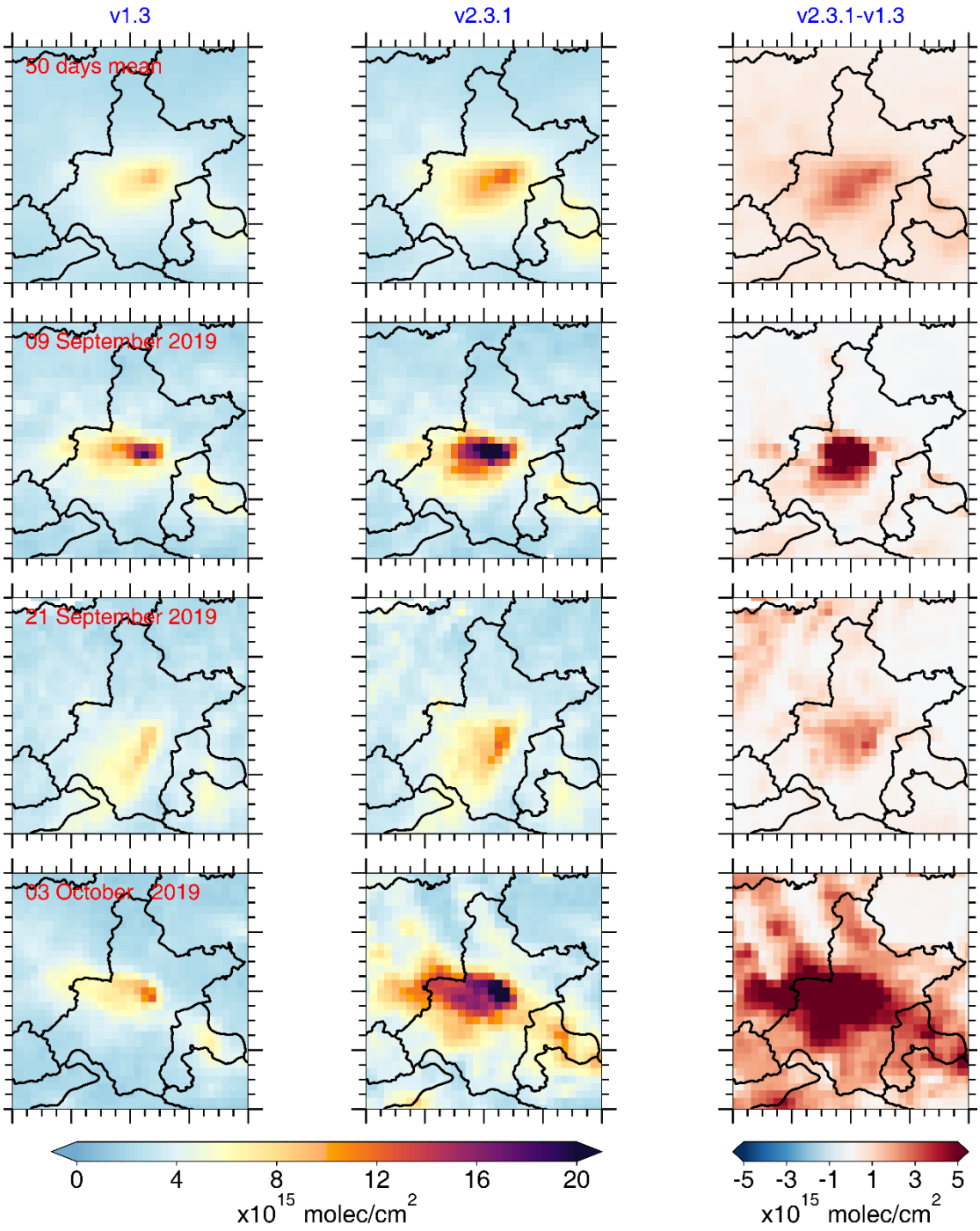

Figure S2: the difference in tropospheric NO_2 column densities between the version 2.3.1 and version 1.3 of TROPOMI data. From top to bottom: the 50 valid days mean in the study period, 09, 21 September and 03 October 2019.

2. Data input into the model besides satellite data and bottom-up emissions

We use the 12.1 version of GEOS-Chem model, with a horizontal resolution 0.25° × 0.3125° (~ 30 × 37.5 km^2) to provide the a priori guesses for chemical parameters relevant to daytime NO_x. The satellite overpasses at around 13:30 local time, when NO_2 is mainly subject to first-order loss with reaction to the hydroxyl radical (OH). The loss rate for NO_x is expressed as $k = \frac{k' \times [OH]}{[NO_x]/[NO_2]}$, where k' is the first-order reaction rate constant (2.8×10^{-11} cm^3/molec/s according to the GEOS-Chem model), $[NO_x]/[NO_2]$ is the mean ratio between NO_x and NO_2 within the boundary layer. We calculated from GEOS-Chem the boundary layer mean NO_x/NO_2 ratio over Wuhan to be 1.26 from September 2019 to August 2020 over Wuhan, and use the annual mean value 1.26 in the fitting, and it is close to that used in Liu et al. (2016) (1.32).

The OH concentration is highly uncertain and in-situ observations are sparse. In this study, we use GEOS-Chem model simulated boundary layer mean OH concentration at 13:00 local time as our first guess and allow it to change by ±20% in the fitting procedure. In addition, OH simulations from the CMAQ model that has a higher spatial resolution are used as a reference. The fraction of boundary layer NO_2 columns of the tropospheric total is also from GEOS-Chem and places typically about 90% of tropospheric NO_2 columns within the boundary layer. Typically, in the daytime, NO_x are mainly subjected to photochemical reaction with the hydroxyl radical (OH) to produce nitric acid (HNO_3), which is quickly converted to nitrate aerosols (NO_3^-). In some rural regions with substantial VOCs emissions, NO_x may also react with VOCs: $CH_3O_2 + NO_2 + M <-> PAN + M$ (e. g. Fischer et al., 2014). We have compared the GEOS-Chem model simulated HNO_3+NO_3^- and PAN concentrations over our study domain in daytime:

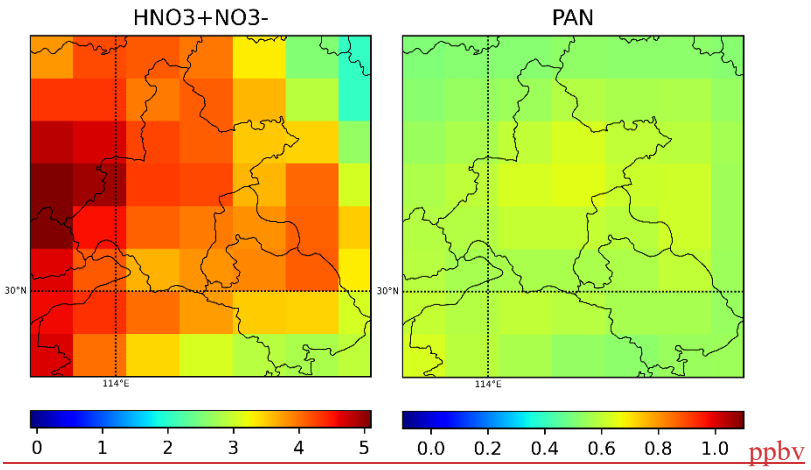

Figure S3: GEOS-chem model simulated monthly mean HNO3+NO3- (left) and PAN (right) concentration for July 2020.

The modeled HNO_3+NO_3^- concentration is 5-10 times higher than PAN over Wuhan, indicating that NO_x loss via OH is the driving pathway of NO_x chemistry over our study domain in the daytime.

At night, NO_2 is oxidized to HNO_3 through the formation of N_2O_5 and NO_3 and heterogeneous reactions including water vapor and aerosols (Shah et al., 2020; Lamsal et al., 2010). The overpass time of the satellite is 13:00–13:30 local time when NO_x chemistry over the city is dominated by the photochemical process, so we consider the reaction between NO_x and OH in the superposition column model as the main loss pathway.

Boundary layer mean wind fields are from ERA5, the fifth generation ECMWF atmospheric reanalysis of the global climate (Hersbach et al., 2020). We use the 05:00 UTC time (13:00 Wuhan time) zonal and meridional winds, with a horizontal resolution of 0.25° × 0.25°. Mean wind speed within boundary layer is calculated using the average of the wind speeds at all vertical layers within the boundary layer weighted by the NO_2 columns within each vertical layer. ~~Considering that the wind field has a strong influence on the distribution of NO_2 column patterns, and thus on the NO_x emission estimation, we filter the TROPOMI NO_2 data based on the wind fields. After excluding the days with fluctuating wind direction (if wind direction changes more than 45 degrees in the hours before TROPOMI overpass) within the study domain, we finally obtain 50 days out of the ensemble of 81 valid satellite days between 1 September 2019 to 31 August 2020 to estimate NO_x and CO_2 emissions from Wuhan. The fraction of~~

~~useful days is comparable to what Lorente et al. (2019) obtained for Paris, which is 27 days in 5 months.~~

3. NO_2 line density

This part demonstrates the way to achieve the 1-D distribution of satellite observed NO_2 along wind direction. First, we define the study domain, the red circle in Fig. S3, including the whole area of Wuhan, as well as other small cities around Wuhan (~~The~~the blue circle is the Third Ring Road of Wuhan, ~50% of NO_x emissions in the red circle are within the blue circle). ~~First~~Then, we resample the TROPOMI NO_2 data at 6km×6km spatial resolution and rotating toward the wind direction, for our study domain, we get 31×31 grid cells. Second, we divide the 31×31 grid cells into 31 'line cells' along the wind direction, as shown with the pink grids in Fig. S3. Each cell is 186km wide (perpendicular to wind direction) and 6km long (along wind direction). Third, the NO_2 line density (molec/cm) within each line cell is calculated through accumulating NO_2 column density (molec/cm^2) of all the 31 grid cells within the line cell, then we obtain the NO_2 line density along wind direction as shown in the right panel of Fig. S3.

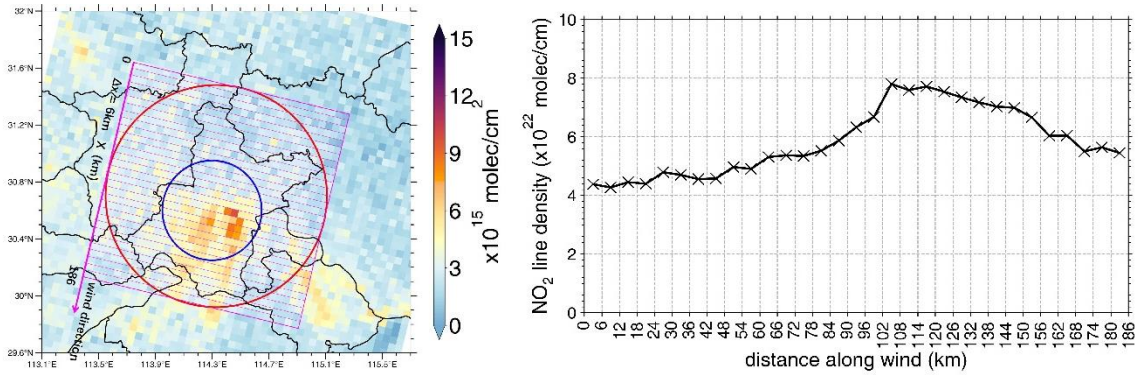

Figure ~~S3~~S4. Left panel: tropospheric NO_2 column on 18 May ~~18th~~ 2020. The data is sampled with 0.05° (lon) × 0.05° (lat) grid size (~6×6km^2) and rotated toward the wind direction. The red circle centered at 114.3°E, 30.7°N represents our study domain, with a diameter of ~186km (31 cells along wind and 31 cells perpendicular to wind), and the blue circle defines the area within the Third Ring Road of Wuhan. For each cell along wind, 31 cells perpendicular to wind are accumulated to make up the line density of NO_2 (right panel).

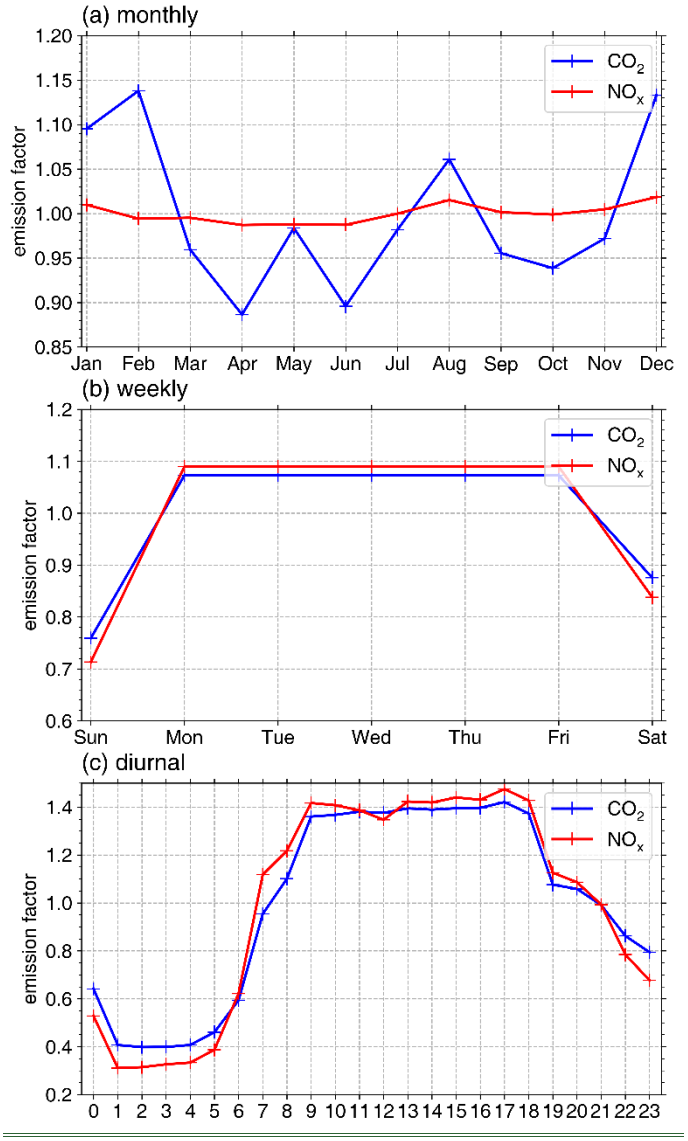

Figure S5. The (a) monthly, (b) weekly and (c) diurnal variation of NO_x and CO_2 emissions from Wuhan. The time factor is provided by ABACAS-EI, MEIC and GEOS-Chem model.

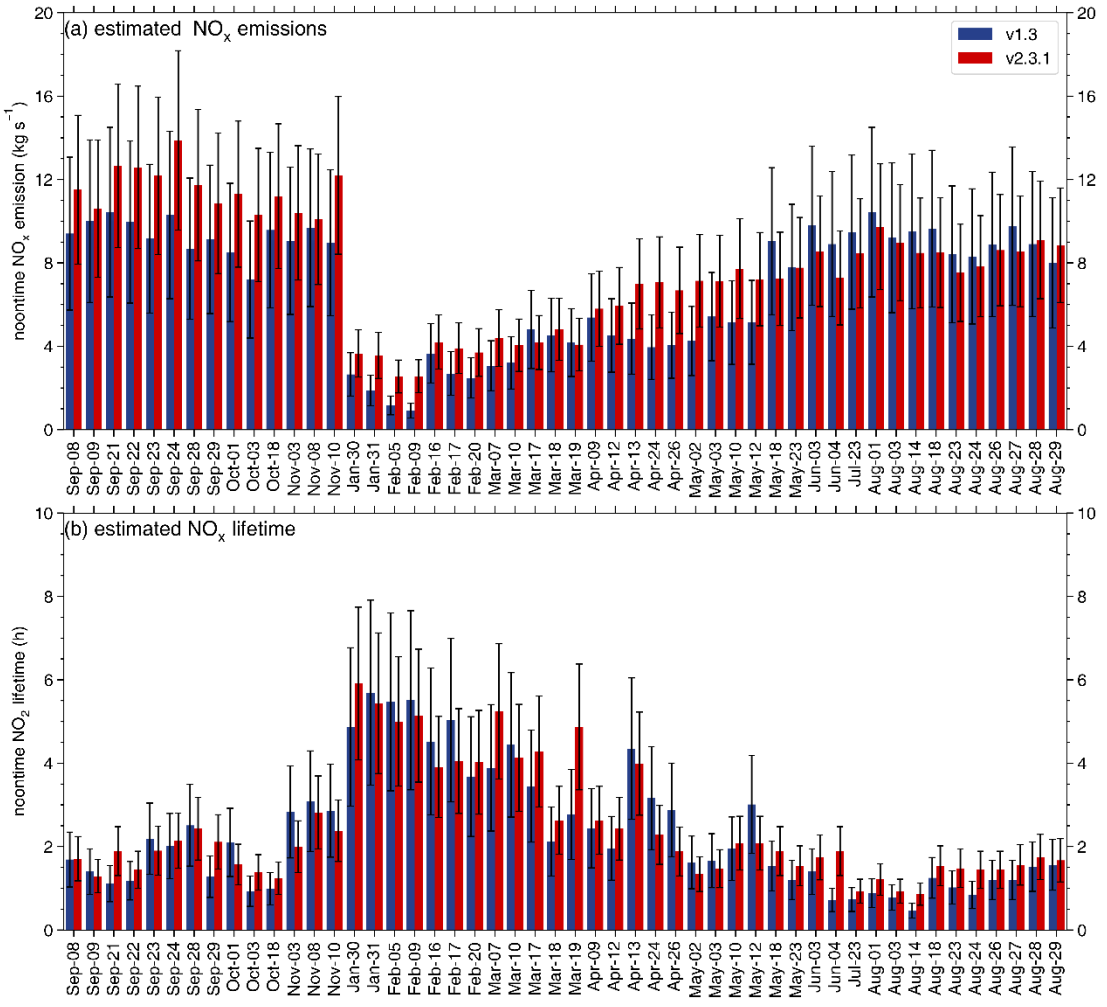

Figure S6. Estimated NO_x (a) emissions and (b) lifetime over Wuhan during the study period based on the TROPOMI-v1.3 (blue bars) and TROPOMI-v2.3.1 (red bars) datasets. The error bars denote the corresponding uncertainty.

4. Robustness with respect to the area of study domain

We choose a relatively large area as our study domain (a circular region centered at 114°E, 30.7°N, with a diameter of ~186km, Fig. S3 left panel, red circle.) to ensure the whole area of Wuhan are included. However, according to the bottom-up emission inventories (Fig. S1), more than 50% of the NO_x emissions in this area are concentrated within the Third Ring Road of Wuhan (84 km diameter, Fig. S3a the blue circle). The large study domain (186km wide of each cell along the NO_2 line density) may smear off the build-up of NO_2 in the high-emission area, and thus impact the estimated NO_x lifetime and emissions. To verify the robustness of our model to the area of the study domain, we randomly choose 3

days (~~08~~8 September 2019, 10 November 2019, and ~~07~~7 March 2020), narrow down the study domain to the blue circle in Fig. ~~S3~~S4. In Fig. S4 we compare NO_x lifetimes and emissions from the inside of the Third Ring Road of Wuhan between the two situations with different area size of study domain. Notably, the NO_2 column density within this smaller domain is higher than outside. The OH radial is the major oxidizing agent to convert primary pollutants to secondary ones in the atmosphere, so the concentration of OH radical concentration is lower inside (Tan et al., 2018). Consequently, lifetime of NO_x inside the smaller domain will be longer.

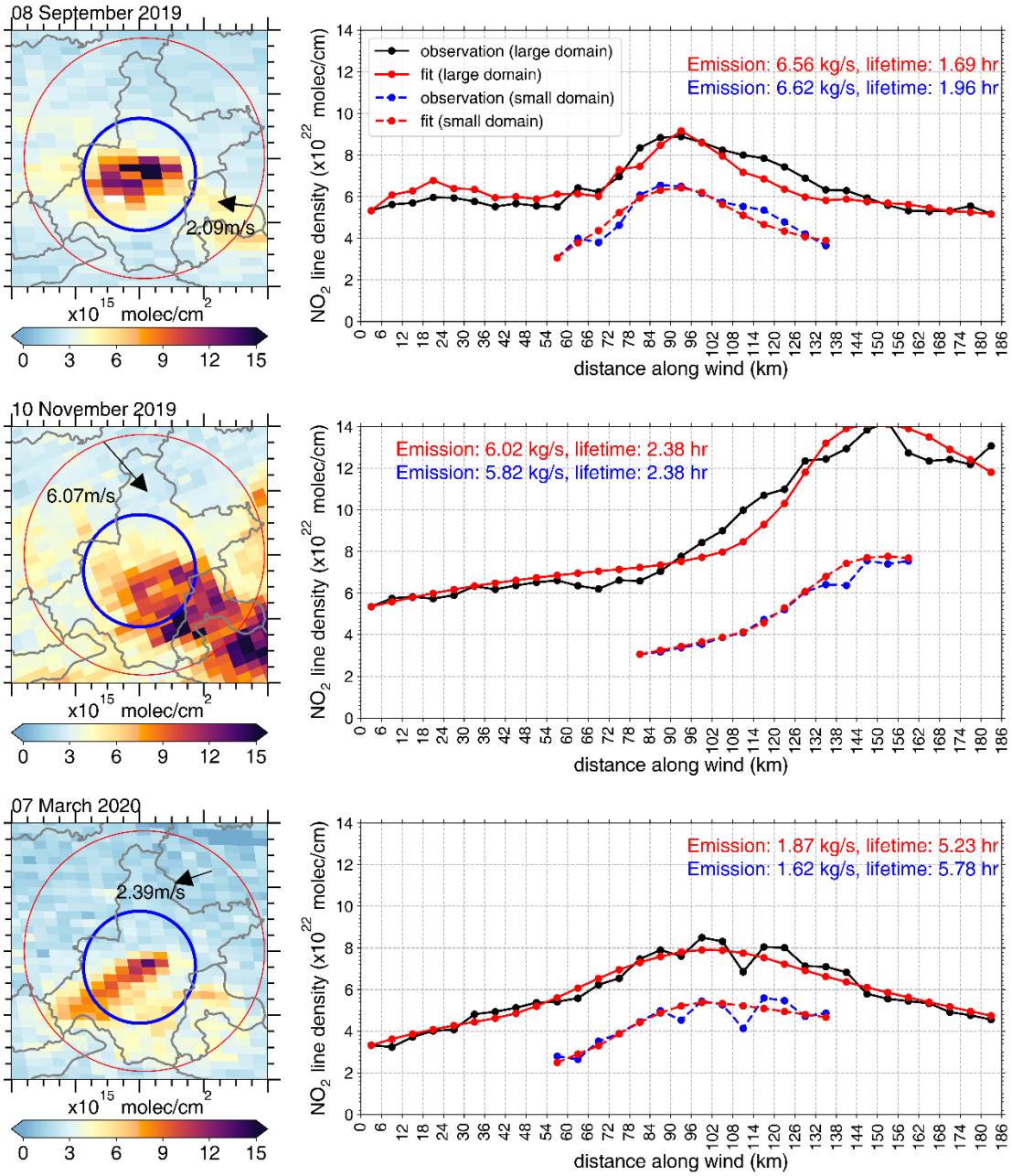

Figure ~~S4~~S7. A comparison of NO_x emissions and lifetimes inside the Third Ring Road of Wuhan (blue circles in the left panel) using the superposition model under the two situations with large (red circles in left panel) and small (blue circles in left panel) study domains. NO_x emissions and lifetimes within the Third Ring Road of Wuhan are listed in right panel.

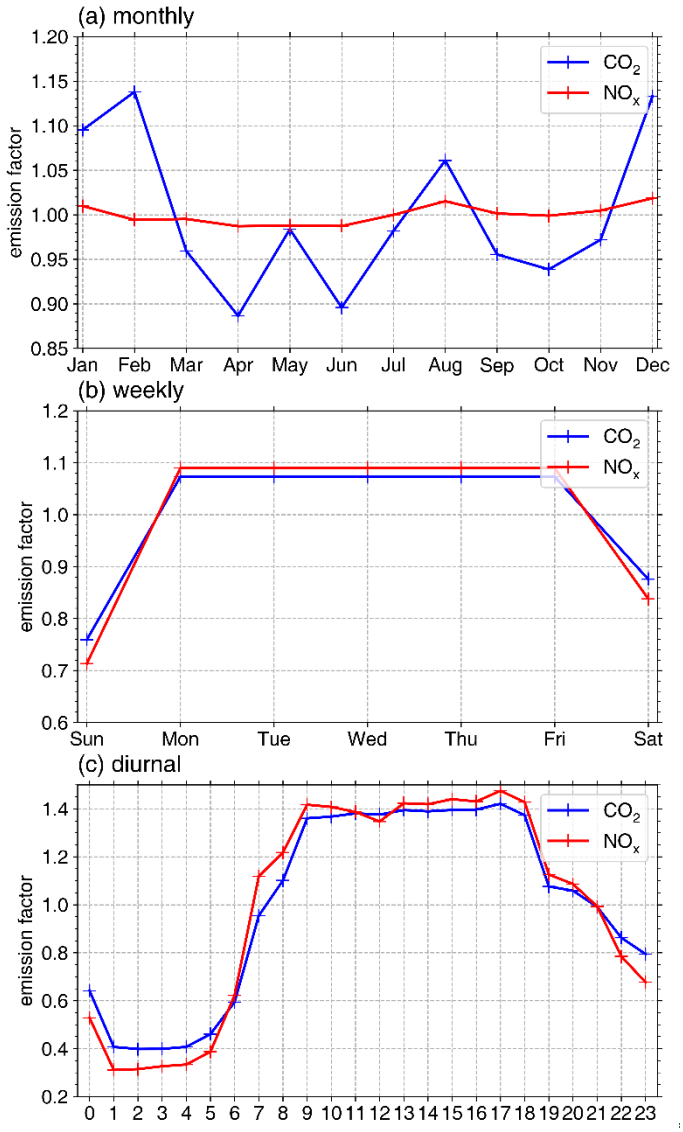

~~**Figure S5.** The (a) monthly, (b) weekly and (c) diurnal variation of NO_x and CO_2 emissions from Wuhan. The time factor is provided by ABACAS-EI, MEIC and GEOS-Chem model.~~

5. The Gaussian plume model

To compare with the results from our superposition column model, we further use a Gaussian plume model (Bovensmann et al., 2010; Zheng et al., 2020) to estimate the XCO_2 enhancement due to Wuhan CO_2 emissions. XCO_2 enhancement on each point of the satellite orbit is contributed from the sum of all CO_2 emissions on the upwind region of the orbit:

$$C_{CO_2} = \sum \frac{E_{CO_2}}{\sqrt{2\pi} \times a \times u \times x^{0.894}} \times EXP[-\frac{1}{2}\left(\frac{y}{a \times x^{0.894}}\right)^2] \quad (1)$$

$$XCO_2 = C_{CO_2} \times \frac{M_{air}}{M_{CO_2}} \times \frac{g}{P_{surf} - w \times g} \times 10^3 \quad (2)$$

In Eq. (1), E_{CO_2} denotes the top-down CO_2 emission (g/s) and C_{CO_2} is the CO_2 column concentration enhancement (g/m^2) relative to the background. u is wind speed in m/s, $x\ (km)$ and $y\ (m)$ are the along wind and across wind distance from the location of the point emission source, respectively. a is the atmospheric stability parameter and the value is taken following Masters and Ela (2007). Eq. (2) is performed to convert C_{CO_2} to XCO_2, in which M_{air} and M_{CO_2} are the molecular weight of air and CO_2, g is the gravitational acceleration $9.8 m/s^2$. P_{surf} is the surface pressure (Pa) and w is the total column water content (kg/m^2), both of which can be accessed from the second Orbiting Carbon Observatory (OCO-2) satellite data file.

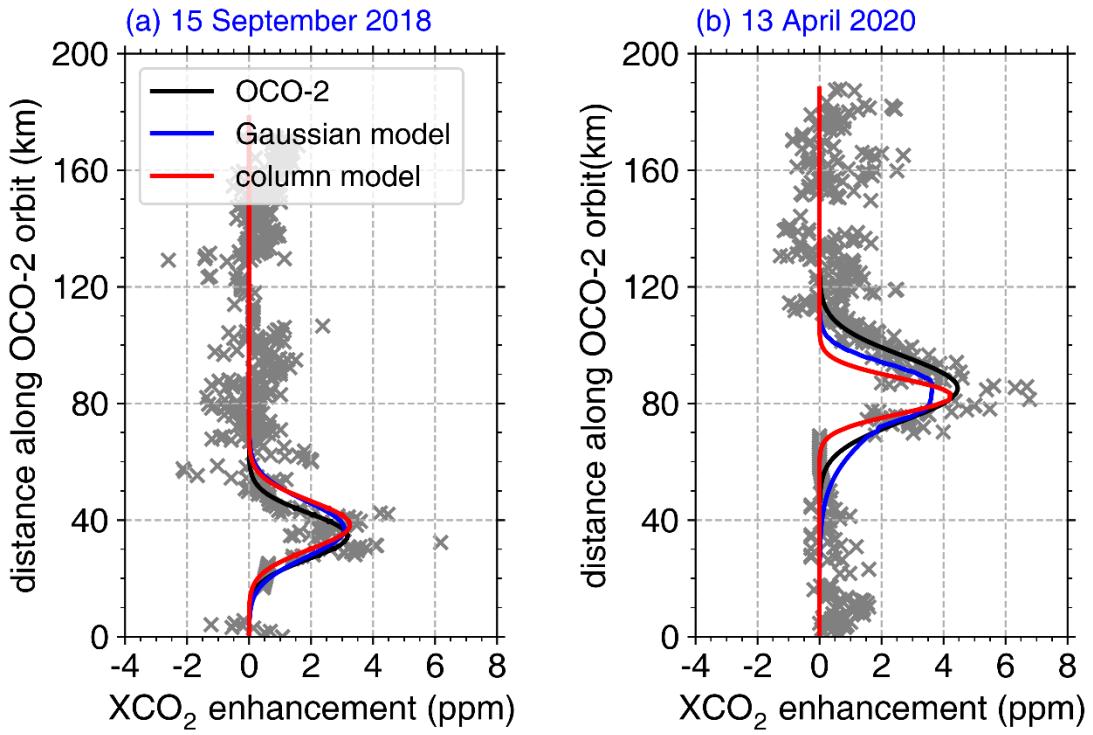

Figure ~~S6~~S8. XCO_2 enhancement observations from OCO-2 (gray dots and black lines), and estimation with our top-down CO_2 emissions from the Gaussian plume model (blue lines) and the superposition model (red lines) on (a) 15 September 2018 and (b) 13 April 2020.

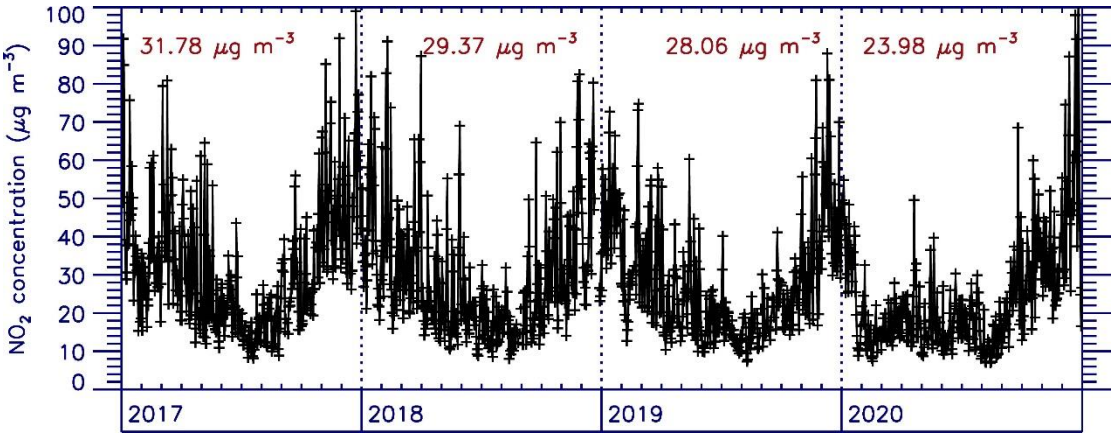

Figure ~~S7~~S9. Daily noontime (13:00 and 14:00 mean) surface observed NO_2 concentration from 2017 to 2020. The annual mean concentration for each year is listed. The data is from the China National Environmental Monitoring Center (CNEMC) network, including 11 sites in Wuhan.

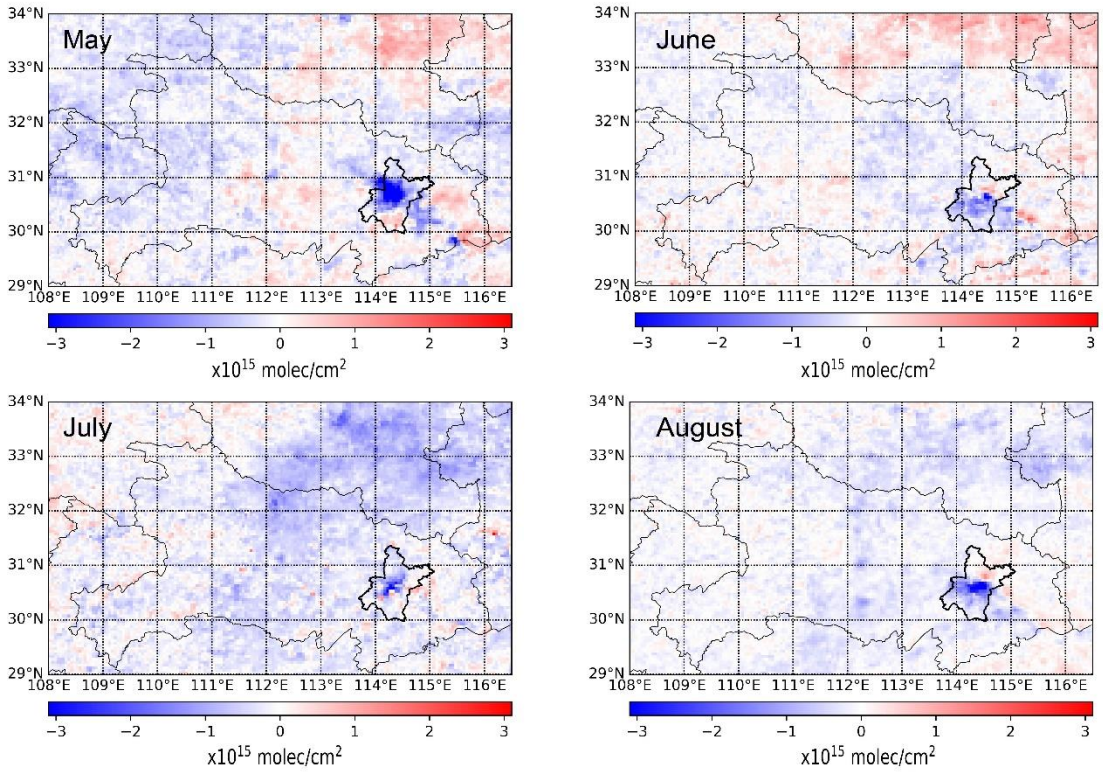

Figure ~~S8~~S10. Difference in monthly mean NO_2 column between 2020 and 2019 (2020 minus 2019) over Hubei Province.

Table S1. NO_x and CO_2 emissions over Wuhan inferred from TROPOMI and related information of 50 days from September 2019 to August 2020.

day		NO_x emission (kg/s)	NO_x lifetime (hrs)	CO_2-to-NO_x Emission ratio (g CO_2/g NO_x)	CO_2 emission (kt/s)	wind speed (m/s)	wind direction (°)	back_offset × 10^{22} molec/cm	back_slope (× 10^{-22} molec/cm^2)	surface temperature (°C)	PBL height (m)	initial GC OH ~~concentraio~~ concentration (molec/cm^3)	initial CMAQ OH concentration (molec/cm^3)	OH concentration best fit (molec/cm^3)	R
2019/9/8	Tue	11.51±~~0.593~~.57	1.71±0.~~10~~53	533±159.9	6.13±~~0.31~~3.00	2.1	59 (ENE)	4.89E+22	-0.002	35	1274	7.63E+06	1.51E+07	7.31E+06	0.91
2019/9/9	Wed	10.~~60±1.026~~±3.29	1.29±0.~~03~~4	533±159.9	5.65±~~0.54~~2.77	2.64	111 (ESE)	4.42E+22	0.001	35	1321	8.17E+06	1.50E+07	9.69E+06	0.96
2019/9/21	Mon	12.65±~~0.933~~.92	1.89±0.~~07~~59	533±159.9	6.74±~~0.53~~.30	10.6	22 (NNE)	4.73E+22	-0.004	27	1652	7.29E+06	1.37E+07	6.61E+06	0.92
2019/9/22	Tue	12.58±~~1.073~~.9	1.44±0.~~03~~45	533±159.9	6.7±~~0.57~~3.28	9.92	29 (NNE)	6.11E+22	-0.01	28	1569	7.97E+06	1.24E+07	8.68E+06	0.95

2019/9/23	Wed	12.18±0.803.78	1.909±0.0859	533±159.9	6.49±0.433.18	6.42	22 (NNE)	3.87E+22	0.005	30	1869	8.35E+06	1.21E+07	6.58E+06	0.97
2019/9/24	Thu	13.88±1.1543	2.14±0.0766	533±159.9	7.4±0.613.63	2.96	40 (NE)	4.96E+22	0.01	30	960	7.29E+06	1.22E+07	5.84E+06	0.96
2019/9/28	Sat	11.73±1.703.64	2.43±0.2975	566±169.8	6.63±0.963.25	2.34	28 (NNE)	5.25E+22	-0.001	32	929	5.97E+06	1.18E+07	5.14E+06	0.98
2019/9/29	Sun (work)	10.86±0.983.37	2.11±0.1365	533±159.9	5.79±0.522.84	2.54	88 E	6.87E+22	-0.002	33	1071	5.95E+06	1.12E+07	5.92E+06	0.92
2019/10/1	Tue (holiday)	11.30±1.933±3.5	1.57±0.1249	533±159.9	6.02±1.032.95	3.29	23 (NNE)	4.32E+22	0	34	862	8.23E+06	1.03E+07	7.96E+06	0.98
2019/10/3	Thu (holiday)	10.30±0.813±3.19	1.38±0.1543	533±159.9	5.48±0.432.69	1.52	175 (S)	6.11E+22	-0.005	32	1203	8.86E+06	1.03E+07	9.06E+06	0.96
2019/10/18	Fri	11.20±1.352±3.47	1.24±0.0638	550±165	6.16±0.743.02	2.94	325 (NW)	4.27E+22	-0.002	27	1343	8.61E+06	6.99E+06	1.01E+07	0.96

2019/11/3	Sun	10.40±0.624 ±3.22	2.00±0.08 62	604±181.2	6.29±0.37 3.08	6.25	359 (N)	5.43E+22	0	26	1231	7.44E+06	6.10E+06	6.25E+06	0.97
2019/11/8	Fri	10.09±1.273 .13	2.82±0.62 87	559±167.7	5.64±0.71 2.76	1.2	53 (NE)	2.74E+22	0	24	1539	5.52E+06	5.46E+06	4.43E+06	0.87
2019/11/10	Sun	12.20±1.232 ±3.78	2.38±0.16 74	604±181.2	7.37±0.74 3.61	6.07	320 (NW)	5.10E+22	-0.001	25	1270	3.59E+06	6.49E+06	5.25E+06	0.97
2020/1/30	Thu (lockdown & holiday)	3.65±0.361. 13	5.91±0261 .83	716±214.8	2.61±0.26 1.28	2.16	343 (NNW)	4.80E+22	-0.02	15	1066	9.77E+05	1.22E+06	2.12E+06	0.96
2020/1/31	Fri (lockdown &	3.56±0.431. 1	5.44±0.15 1.69	716±214.8	2.55±0.31 1.25	2.92	155 (SSE)	5.13E+22	-0.01	14	794	1.91E+06	1.81E+06	2.30E+06	0.85

	holiday)														
2020/2/5	Wed (lockdown)	2.55±0.3179	5.00±0.17±1.55	674±202.2	1.72±0.2184	4.93	105 (ESE)	3.67E+22	0	15	870	3.13E+06	3.14E+06	2.50E+06	0.85
2020/2/9	Sun (lockdown)	2.56±0.3379	5.14±0.181.59	729±218.7	1.86±0.2491	1.44	272 (W)	4.05E+22	-0.005	15	851	3.10E+06	3.30E+06	2.43E+06	0.9
2020/2/16	Sun (lockdown)	4.20±0.522±1.3	3.91±0.351.21	729±218.7	3.06±0.381.50	5.97	336 (NNW)	1.64E+22	-0.01	7	1365	3.34E+06	3.36E+06	3.20E+06	0.96
2020/2/17	Mon (lockdown)	3.91±0.461.21	4.05±0.251.26	674±202.2	2.64±0.311.29	4.56	342 (NNW)	3.32E+22	-0.002	13	1358	3.67E+06	3.45E+06	3.09E+06	0.95
2020/2/20	Thu (lockdown)	3.70±0.457±1.15	4.02±0.221.25	674±202.2	2.49±0.31.22	4.52	124 (SE)	3.48E+22	-0.015	17	956	3.72E+06	4.64E+06	3.11E+06	0.9

2020/3/7	Sat (lockdown)	4.39±0.631.36	5.24±0.271.62	663±198.9	2.91±0.421.43	2.39	72 (ENE)	2.94E+22	-0.02	19	660	2.63E+06	4.73E+06	2.39E+06	0.97
2020/3/10	Tue (lockdown)	4.05±0.561.26	4.13±0.141.28	625±187.5	2.53±0.351.24	4.94	336 (NNW)	3.00E+22	-0.02	18	1173	2.33E+06	6.69E+06	3.03E+06	0.98
2020/3/17	Tue (lockdown)	4.18±0.761.3	4.28±0.121.33	625±187.5	2.61±0.471.28	3.39	273 (W)	2.43E+22	0	21	1356	3.49E+06	7.41E+06	2.92E+06	0.94
2020/3/18	Wed (lockdown)	4.81±0.351.49	2.63±0.0682	625±187.5	3±0.22.00±1.47	5.2	225 (SW)	3.43E+22	-0.01	23	1046	4.37E+06	8.11E+06	4.75E+06	0.92
2020/3/19	Thu (lockdown)	4.08±0.491.26	4.87±0.161.51	625±187.5	2.55±0.311.25	3.2	36 (NE)	3.63E+22	-0.015	23	1057	3.60E+06	8.66E+06	2.57E+06	0.96
2020/4/9	Thu	5.80±0.638±1.8	2.63±0.1182	635±190.5	3.68±0.41.8	3.4	179 (S)	5.06E+22	-0.01	27	1465	4.51E+06	9.69E+06	4.75E+06	0.95

2020/4/12	Sun	5.94±0.241.84	2.43±0.0575	674±202.2	4±0.16.00±1.96	7.43	311 (NW)	4.59E+22	0	21	1948	5.60E+06	1.03E+07	5.14E+06	0.97
2020/4/13	Mon	6.99±0.782.17	3.99±0.221.24	635±190.5	4.44±0.52.18	1.67	272 (W)	5.43E+22	-0.01	22	1719	4.93E+06	9.41E+06	3.13E+06	0.96
2020/4/24	Fri	7.06±0.772.19	2.28±0.0871	635±190.5	4.48±0.492.2	5.39	264 (W)	2.16E+22	0	22	2427	6.58E+06	1.16E+07	5.48E+06	0.92
2020/4/26	Sun (work)	6.68±0.422.07	1.88±0.1858	635±190.5	4.24±0.272.08	5.49	242 (WSW)	3.89E+22	0.001	27	1282	6.45E+06	1.36E+07	6.65E+06	0.89
2020/5/2	Sat (holiday)	7.14±0.972.21	1.34±0.1342	628±188.4	4.48±0.612.20	6.49	238 (WSW)	4.73E+22	-0.01	26	944	8.02E+06	1.75E+07	9.33E+06	0.91
2020/5/3	Sun (holiday)	7.12±0.872.21	1.47±0.0346	640±192	4.55±0.562.23	4.35	198 (SSW)	4.10E+22	-0.005	27	1312	7.80E+06	1.85E+07	8.50E+06	0.97
2020/5/10	Sun	7.72±0.912.39	2.08±0.1164	640±192	4.94±0.582.42	3.42	324 (NW)	1.44E+22	0.002	27	1370	7.51E+06	1.48E+07	6.01E+06	0.97

2020/5/12	Tue	7.22±0.592.24	2.08±0.0964	592±177.6	4.27±0.352.09	4.1	297 (WNW)	1.56E+22	-0.005	30	1693	5.93E+06	1.41E+07	6.01E+06	0.89
2020/5/18	Mon	7.23±1.262.24	1.89±0.2459	592±177.6	4.28±0.752.10	6.91	8 (N)	4.26E+22	-0.005	36	1546	7.55E+06	1.61E+07	6.61E+06	0.96
2020/5/23	Sat	7.77±0.392.41	1.54±0.1048	628±188.4	4.88±0.242.39	3.51	197 (SSW)	4.01E+22	-0.01	35	1521	8.36E+06	1.78E+07	8.12E+06	0.96
2020/6/3	Wed	8.56±1.022.65	1.74±0.1654	530±159	4.54±0.542.22	2.29	107 (ESE)	3.67E+22	0	31	969	9.22E+06	1.16E+07	7.18E+06	0.96
2020/6/4	Thu	7.28±0.882.26	1.89±0.2259	530±159	3.86±0.471.89	4.54	215 (SW)	2.05E+22	-0.01	33	1350	9.95E+06	1.50E+07	6.61E+06	0.95
2020/7/23	Thu	8.45±0.252.62	0.93±0.0429	518±155.4	4.38±0.132.15	4.99	240 (WSW)	2.49E+22	-0.005	34	1040	1.23E+07	1.82E+07	1.34E+07	0.87
2020/8/1	Sat	9.73±1.153.02	1.21±0.1238	619±185.7	6.02±0.712.95	4.34	205 (SSW)	3.62E+22	-0.02	34	977	1.02E+07	2.06E+07	1.03E+07	0.93
2020/8/3	Mon	8.97±1.052.78	0.93±0.1229	583±174.9	5.23±0.612.56	4.4	201 (SSW)	2.96E+22	-0.02	37	1104	1.15E+07	2.14E+07	1.34E+07	0.94

2020/8/14	Fri	8.48±0.842.63	0.86±0.0627	583±174.9	4.94±0.492.42	8.38	213 (SSW)	2.52E+22	-0.02	36	961	9.74E+06	2.03E+07	1.45E+07	0.93
2020/8/18	Tue	8.49±0.742.63	1.54±0.1948	583±174.9	4.95±02.43	2.97	191 (S)	3.55E+22	-0.005	35	1151	7.17E+06	2.04E+07	8.12E+06	0.95
2020/8/23	Sun	7.52±0.992.33	1.48±0.0546	630±189	4.74±0.622.32	3.86	193 (SSW)	3.01E+22	-0.02	32	941	5.62E+06	1.69E+07	8.45E+06	0.93
2020/8/24	Mon	7.84±0.662.43	1.44±0.1845	583±174.9	4.57±0.382.24	6.87	241 (WSW)	2.75E+22	-0.02	34	1020	7.68E+06	1.88E+07	8.68E+06	0.91
2020/8/26	Wed	8.61±1.132.67	1.44±0.1345	583±174.9	5.02±0.662.46	5.19	340 (NNW)	3.08E+22	0	31	1039	1.08E+07	1.55E+07	8.68E+06	0.96
2020/8/27	Thu	8.55±0.662.65	1.56±0.0548	583±174.9	4.98±0.382.44	2.52	42 (NE)	3.48E+22	0	33	841	9.59E+06	1.45E+07	8.01E+06	0.95
2020/8/28	Fri	9.10±0.841±2.82	1.75±0.2354	583±174.9	5.3±0.4930±2.6	2.37	46 (NE)	3.81E+22	0	33	1089	8.54E+06	1.71E+07	7.14E+06	0.93
2020/8/29	Sat	8.85±0.722.74	1.67±0.2452	619±185.7	5.47±0.452.68	4.39	36 (NE)	3.13E+22	0	33	1028	7.39E+06	1.72E+07	7.49E+06	0.94

Table S2. Uncertainty of each factors and their influence on NO_x and CO_2 emission estimation..

factor	uncertainty	Influence on NO_x and (or) CO_2 emissions
Satellite NO_2 retrieval	±20 %	20 %
OH concentration	±20 %	3 %
NO_2/NO_x ratio	±10 %	8 %
Wind field	±20 %	17 %
Area of study domain	/	15 %
CO_2-to-NO_x emission ratio	±30 %	30 %

References

Bovensmann, H., Buchwitz, M., Burrows, J. P., Reuter, M., Krings, T., Gerilowski, K., Schneising, O., Heymann, J., Tretner, A., and Erzinger, J.: A remote sensing technique for global monitoring of power plant CO_2 emissions from space and related applications, Atmos. Meas. Tech., 3, 781-811, 10.5194/amt-3-781-2010, 2010.

Fischer, E. V., Jacob, D. J., Yantosca, R. M., Sulprizio, M. P., Millet, D. B., Mao, J., Paulot, F., Singh, H. B., Roiger, A., Ries, L., Talbot, R. W., Dzepina, K., and Pandey Deolal, S.: Atmospheric peroxyacetyl nitrate (PAN): a global budget and source attribution, Atmos. Chem. Phys., 14, 2679-2698, 10.5194/acp-14-2679-2014, 2014.

Hersbach, H., Bell, B., Berrisford, P., Hirahara, S., Horányi, A., Muñoz‐Sabater, J., Nicolas, J., Peubey, C., Radu, R., Schepers, D., Simmons, A., Soci, C., Abdalla, S., Abellan, X., Balsamo, G., Bechtold, P., Biavati, G., Bidlot, J., Bonavita, M., Chiara, G., Dahlgren, P., Dee, D., Diamantakis, M., Dragani, R., Flemming, J., Forbes, R., Fuentes, M., Geer, A., Haimberger, L., Healy, S., Hogan, R. J., Hólm, E., Janisková, M., Keeley, S., Laloyaux, P., Lopez, P., Lupu, C., Radnoti, G., Rosnay, P., Rozum, I., Vamborg, F., Villaume, S., and Thépaut, J. N.: The ERA5 global reanalysis, Q J R Meteorol Soc., 146, 1999-2049, 10.1002/qj.3803, 2020.

Lamsal, L. N., Martin, R. V., van Donkelaar, A., Celarier, E. A., Bucsela, E. J., Boersma, K. F., Dirksen, R., Luo, C., and Wang, Y.: Indirect validation of tropospheric nitrogen dioxide retrieved from the OMI satellite instrument: Insight into the seasonal variation of nitrogen oxides at northern midlatitudes, J. Geophys. Res., 115, 10.1029/2009jd013351, 2010.

Liu, F., Beirle, S., Zhang, Q., Dörner, S., He, K., and Wagner, T.: NO_x lifetimes and emissions of cities and power plants in polluted background estimated by satellite observations, Atmos. Chem. Phys., 16, 5283-5298, 10.5194/acp-16-5283-2016, 2016.

~~Lorente, A., Boersma, K. F., Eskes, H. J., Veefkind, J. P., van Geffen, J., de Zeeuw, M. B., Denier van der Gon, H. A. C., Beirle, S., and Krol, M. C.: Quantification of nitrogen oxides emissions from build-up of pollution over Paris with TROPOMI, Sci. Rep., 9, 20033, 10.1038/s41598-019-56428-5, 2019.~~

Masters, G. M. and Ela, W. P.: Introduction to environmental engineering and science, Pearson, 3rd edition pp. 457, 2007.

Shah, V., Jacob, D. J., Li, K., Silvern, R. F., Zhai, S., Liu, M., Lin, J., and Zhang, Q.: Effect of changing NO_x lifetime on the seasonality and long-term trends of satellite-observed tropospheric NO_2 columns over China, Atmos. Chem. and Phys., 20, 1483-1495, 10.5194/acp-20-1483-2020, 2020.

Tan, Z., Rohrer, F., Lu, K., Ma, X., Bohn, B., Broch, S., Dong, H., Fuchs, H., Gkatzelis, G. I., Hofzumahaus, A., Holland, F., Li, X., Liu, Y., Liu, Y., Novelli, A., Shao, M., Wang, H., Wu, Y., Zeng, L., Hu, M., Kiendler-Scharr, A., Wahner, A., and Zhang, Y.: Wintertime photochemistry in Beijing: observations of RO_x radical concentrations in the North China Plain during the BEST-ONE campaign, Atmospheric Chemistry and Physics, 18, 12391-12411, 10.5194/acp-18-12391-2018, 2018.

Zheng, B., Chevallier, F., Ciais, P., Broquet, G., Wang, Y., Lian, J., and Zhao, Y.: Observing carbon dioxide emissions over China's cities and industrial areas with the Orbiting Carbon Observatory-2, Atmos. Chem. Phys., 20, 8501-8510, 10.5194/acp-20-8501-2020, 2020.